



TECHNISCHE
UNIVERSITÄT
WIEN
Vienna University of Technology

DIPLOMARBEIT

Robust coherent optimal control of nitrogen-vacancy quantum bits in diamond

ausgeführt am Atominstitut der Technischen Universität Wien
unter der Anleitung von

Univ. Prof. Dr. Hannes-Jörg Schmiedmayer
Univ. Ass. Dr. Johannes Majer
Projektassistent Dr. Tobias Nöbauer

eingereicht an der
Technischen Universität Wien
Fakultät für Physik

von

Andreas Angerer
Matrikelnummer 0727110
Hauffgasse 8/3/16, 1110 Wien

Wien, am 31. Dezember 2013

Abstract

During the last ten years, basic quantum operations on a single electronic spins in the nitrogen-vacancy defect center in diamond have been a rich field of study. Quantum operations coherently manipulating the spin of the nitrogen-vacancy center have become promising candidates for easy to manipulate qubits. However in order to implement these qubits in quantum computers robust high-fidelity control is needed.

Building on an existing confocal microscopy setup, pulsed and quadrature-amplitude modulated microwave signals were used to realize coherent spin manipulation measurements. Especially designed Smooth Optimal Control pulses (robust against detuning and different control amplitudes) were used to develop measurement schemes resulting in the aforementioned increase of fidelity.

The first part of the thesis describes the implementation of these pulses into the existing experimental setup and the calibration work necessary prior to measurements, due to imperfections of devices in the microwave chain.

The second part is dedicated to the analysis of the pulses applied to a single spin by comparing the experimental results to theoretical simulations. This was done not only for one resonant spin with accurate control amplitude, but also for a range of different detunings and amplitudes. A more thorough analysis of the pulses was then achieved by using state/process tomography, resulting in a complete description of the process induced by these optimized pulses.

Finally, after verifying the effect of the pulses, measurement schemes for sensing alternating magnetic fields were implemented, resulting in measurements with improved sensitivity for magnetic fields.

Contents

| | |
|---|-----------|
| Abstract | c |
| 1 Introduction | 1 |
| 2 Basic physics of the NV-center | 3 |
| 2.1 Quantum theory of the two-level system | 3 |
| 2.1.1 Representation on the Bloch-sphere | 5 |
| 2.1.2 Single qubit operations | 6 |
| 2.2 Structure of the NV-center | 7 |
| 2.3 Spin properties of the NV-center and optical transitions | 8 |
| 2.3.1 Optical transitions | 10 |
| 2.3.1.1 Coupling to phonons | 10 |
| 2.3.1.2 Fluorescence time traces and spin polarization | 10 |
| 2.4 Fine- and hyperfine structure and transitions in the ground-state | 12 |
| 3 Experimental setup and measurement schemes | 15 |
| 3.1 Confocal microscope | 15 |
| 3.2 Electron spin resonance experiments | 16 |
| 3.2.1 Microwave chain | 16 |
| 3.2.2 Coils | 17 |
| 3.2.3 Dephasing and loss of coherence | 18 |
| 3.2.4 ODMR | 19 |
| 3.2.5 Pulsed measurements | 20 |
| 3.2.5.1 Rabi nutations | 21 |
| 3.2.5.2 Free induction decay measurements | 22 |
| 3.2.5.3 Spin-echo measurements | 22 |
| 4 Implementing smooth optimal control | 27 |
| 4.1 Theory | 27 |
| 4.1.1 Simulating the dephasing environment | 30 |
| 4.2 IQ-Mixer calibration | 34 |
| 4.3 Single NV measurements | 39 |
| 4.3.1 Measurement sequence | 40 |
| 4.3.2 “Spin-selection” scheme | 40 |
| 4.3.3 Experimental data versus simulation | 41 |

| | | |
|----------|--|-----------|
| 4.3.4 | Fidelity plot | 42 |
| 4.3.5 | State/process tomography | 44 |
| 4.4 | NV ensemble measurements | 53 |
| 4.4.1 | Power and squeeze-scans | 53 |
| 4.4.2 | Spin-echo measurements using Smooth Optimal Control-pulses | 56 |
| 5 | Magnetometry using smooth optimal control | 59 |
| 5.1 | Interferometric magnetic sensing using spin-echo sequences | 59 |
| 5.1.1 | Minimum detectable magnetic field | 60 |
| 5.1.2 | Sensing using smooth optimal control | 62 |
| 5.2 | Wide-field magnetic sensing | 64 |
| 6 | Conclusion and outlook | 67 |
| | Bibliography | 69 |
| | List of Figures | 75 |
| | Acknowledgments | 81 |

1 Introduction

Not only because of its rareness and preciousness diamond is of special interest, but also for implementing quantum information processing architectures and sensing magnetic fields at unprecedented resolution. All of this is made possible by one impurity, namely the nitrogen-vacancy (NV) center, which has attracted the attention of physicists within the last 50 years.

This defect center shows remarkable behavior in many respects: It is a quantum system with two distinct states, very well suited for quantum information processing. It is a source of fluorescence where the two distinct quantum states may easily be identified using the difference in fluorescence intensity of the two states. Moreover it shows practically no photo-bleaching and is mechanically inherently stationary [Fu07]. Although it is very stable it is still sensitive to external electric and magnetic fields. The NV center is a single photons source emitting only one photon at a time but with a very high fluorescence rate of about $77\,000\text{ s}^{-1}$ [Man06], roughly in the same range as quantum dots. Aside from these quite positive characteristics, the most remarkable aspect of the nitrogen-vacancy center is probably the fact that despite being embedded into the room-temperature environment of diamond it is capable of storing quantum information for several hundreds of microseconds, or even longer. Thus the NV-center may be a promising candidate to build quantum computers, providing stable and easy to read out quantum states with long coherence times [Maj07]. The nitrogen-vacancy center may also be a promising candidate for scalable quantum computers, by coupling it to a grid of optical cavities or superconducting qubits [Lep11].

This thesis does not primarily deal with manipulation of single NV centers, but with experiments with a lot of NV centers at a time. Using more NV-centers provides advantages when doing magnetometry and it offers the possibility to store quantum information in the collective state of an NV ensemble. This comes at the expense of having to work with an experimental system not as intuitive and less well-defined than a single NV center. Especially inhomogeneous broadening, due to not fully understood dipole-dipole interactions and inhomogeneities in the surrounding spin-bath makes it very hard to implement quantum gates with sufficient fidelity.

Therefore a new promising set of optimal control pulses was developed by our collaborators in Freiburg (namely Dr. Florian Mintert et. al) [Bar13], generating smooth quadrature modulated pulses within a well-defined bandwidth, robust for this kind of inhomogeneities and yielding highly efficient quantum gates.

The first part of this thesis concentrates on the basic physics concerning NV-centers, describing it as a two-level system and showing how to represent its states on the

Bloch-sphere.

It is followed by a part introducing the whole experimental setup used to detect fluorescence of the NV-center as well as coherent spin manipulation using microwave pulses.

The scope of this thesis was to show the implementation and verification of the smooth optimal control pulses, and finally to introduce a magnetic sensing scheme using the advantages of the pulses to create robust measurements with a very high sensitivity. The implementation and results are presented in chapter [4](#) and [5](#).

2 Basic physics of the NV-center

2.1 Quantum theory of the two-level system

In quantum mechanics, a two-level system is a simple, but powerful model-system capable of describing a lot of fundamental quantum physical properties.

Formally described, the Hilbert space of a two-level system has two degrees of freedom, therefore a complete basis is described by two linearly independent states [Coh05]. As an example one can consider an atom (or in our case a nitrogen vacancy-center) with two non-degenerate eigenstates, namely the ground- and excited state (which we name $|0\rangle$ and $|1\rangle$).

The situation is depicted in Fig. 2.1, with ω being the transition frequency, Δ the detuning and ω_0 the resonance frequency. $|0\rangle$ and $|1\rangle$ form an orthonormal basis for the system. If there is no driving field present, states $|0\rangle$ and $|1\rangle$ are obviously the eigenstates of the system, with eigenvalues (hence energies) 0 and $\hbar\omega_0$. The state of a two-level system can now be expressed as a coherent superposition of the two eigenstates $|\Psi(t)\rangle = c_0|0\rangle + c_1|1\rangle e^{-i\omega_0 t}$ where c_0 and c_1 are two complex state amplitudes

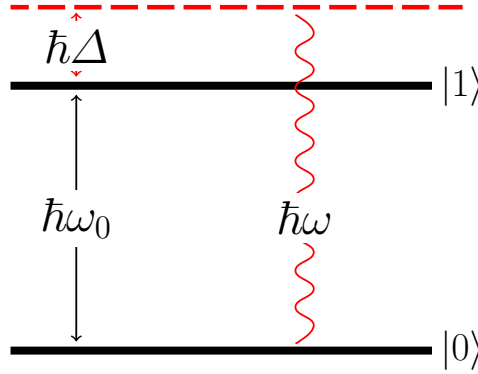


Fig. 2.1

which have to fulfill the normalization $|c_0|^2 + |c_1|^2 = 1$. Turning on a driving field a transition between the $|0\rangle$ and $|1\rangle$ state is induced, so that the Hamiltonian changes from the bare Hamiltonian \hat{H}_0 to a Hamiltonian with an interaction term $\hat{H} = \hat{H}_0 + \hat{V}(t)$. Since the states $|i\rangle$ form a complete basis set, it is still possible to write the general state as $|\Psi(t)\rangle = c_0(t)|0\rangle + c_1(t)|1\rangle e^{-i\omega_0 t}$. The whole problem reduces now to finding the time-behavior of the coefficients c_0 and c_1 . Substituting this into the Schrödinger equation $\hat{H}|\Psi\rangle = i\hbar\frac{\partial\Psi}{\partial t}$ one finds after simple algebraic operations [Fox06], for both coefficients

$$\dot{c}_0(t) = -\frac{i}{\hbar} (c_0(t)V_{11} + c_1(t)V_{12}(t)e^{-i\omega_0 t}) \quad (2.1)$$

$$\dot{c}_1(t) = -\frac{i}{\hbar} (c_0(t)V_{21}e^{-i\omega_0 t} + c_1(t)V_{22}(t)) \quad (2.2)$$

where $V_{ij}(t) = \langle i | V(t) | j \rangle$. To investigate this further, one needs to know the exact form of $V(t)$. Using a semi-classical approach, the energy-shift induced by the atom-light interaction is given by [Fox06]

$$\hat{V}(t) = e\mathbf{r}\mathcal{E}(t) \quad (2.3)$$

describing the energy of an electric dipole in an electric field. Arbitrarily defining the z-axis as the direction of the polarization of the light-field, gives then

$$\hat{V}(t) = ez\mathcal{E}_0 \cos(\omega t) = \frac{ez\mathcal{E}_0}{2} (e^{i\omega t} + e^{-i\omega t}) \quad (2.4)$$

and thus

$$\hat{V}_{ij}(t) = -\frac{\mathcal{E}_0}{2} (e^{i\omega t} + e^{-i\omega t}) \mu_{ij} \quad (2.5)$$

with $\mu_{ij} = -e \langle i | z | j \rangle$ being the dipole matrix-element. Since the position operator z has odd parity and atomic states always have either even or odd parity it follows that $\mu_{ii} = 0$. Moreover the dipole moment is a measurable quantity, hence it has to be a real variable, and $\mu_{12} = \mu_{21}$. This results in the simplified rate equations

$$\dot{c}_0(t) = \frac{i}{2}\Omega_R \left(e^{i(\omega-\omega_0)} + e^{-i(\omega+\omega_0)} \right) c_1(t) \quad (2.6)$$

$$\dot{c}_1(t) = \frac{i}{2}\Omega_R \left(e^{-i(\omega-\omega_0)} + e^{i(\omega+\omega_0)} \right) c_0(t) \quad (2.7)$$

with the Rabi-frequency $\Omega_R = |\mu_{12}\mathcal{E}_0/\hbar|$.

Solving these differential equations gives us the desired parameters to understand the time-dependent behavior of the two-level system. This can be done in a simple way for the two extreme cases known as the low- and the strong-field limit. Since we aim at changing the spin of the electron as fast as possible, we are interested in the strong-field limit.

In order to solve the differential equations in the strong field limit, we need to make an assumption known as rotating-wave approximation (RWA), which means that we neglect all fast oscillating terms $\omega + \omega_0$. This is a valid approximation if $\Delta \ll \omega + \omega_0$ and hence the fast oscillating terms average to zero on an appreciable time-scale much faster than any observation we can carry out. Moreover assuming a resonant driving field ($|\omega - \omega_0| = 0$), Eq. 2.6 and Eq. 2.7 reduce to

$$\dot{c}_0(t) = \frac{i}{2}\Omega_R c_1(t) \quad (2.8)$$

$$\dot{c}_1(t) = \frac{i}{2}\Omega_R c_0(t) \quad (2.9)$$

It is now straightforward to solve these equations, with solutions

$$c_0(t) = \cos\left(\frac{\Omega_R t}{2}\right) \quad (2.10)$$

$$c_1(t) = i \sin\left(\frac{\Omega_R t}{2}\right) \quad (2.11)$$

The time-dependent probabilities of finding the electron in one of the two states are then given by

$$\mathcal{P}_{|0\rangle}(t) = |c_0(t)|^2 = \cos^2\left(\frac{\Omega_R t}{2}\right) \quad (2.12)$$

$$\mathcal{P}_{|1\rangle}(t) = |c_1(t)|^2 = \sin^2\left(\frac{\Omega_R t}{2}\right) \quad (2.13)$$

At $t = \pi/\Omega_R$ (π -pulse) the spin is in the upper level, whereas at $t = \pi/2\Omega_R$ ($\pi/2$ -pulse), we have a superposition between the two states (for the descriptions in terms of quantum information see Sec. 2.1.2). If the driving field is off-resonant, one has to define an effective Rabi-frequency $\Omega^2 = \Omega_R^2 + \Delta^2$ and scale the transition probabilities with this parameter, such that [Coh05]

$$\mathcal{P}_{|1\rangle}(t) = \frac{\Omega_R^2}{\Omega^2} \sin^2\left(\frac{\Omega t}{2}\right) \quad (2.14)$$

$$\mathcal{P}_{|0\rangle}(t) = 1 - \mathcal{P}_{|1\rangle}(t). \quad (2.15)$$

2.1.1 Representation on the Bloch-sphere

A very intuitive yet very use- and powerful visualization of the two-level system is the so called Bloch-sphere. Given two eigenstates $|0\rangle$ and $|1\rangle$ every possible state is given by a linear combination of the two states $|\Psi\rangle = \alpha|0\rangle + \beta|1\rangle$ with $|\alpha|^2 + |\beta|^2 = 1$ and $\alpha, \beta \in \mathbb{C}$ [Nie00]. Since α and β are complex numbers, and the global phase can be neglected (because it has no effect on observables), this equation may be rewritten to

$$|\Psi\rangle = \cos\left(\frac{\theta}{2}\right)|0\rangle + e^{i\phi}\sin\left(\frac{\theta}{2}\right)|1\rangle \quad (2.16)$$

where θ and ϕ define a point on a unit three-dimensional sphere, or Bloch-sphere. Although there is no simple generalization for multiple qubits, the Bloch sphere is still very useful in a lot of cases, when dealing with single NVs (as often in our case) or very few spins at a time.

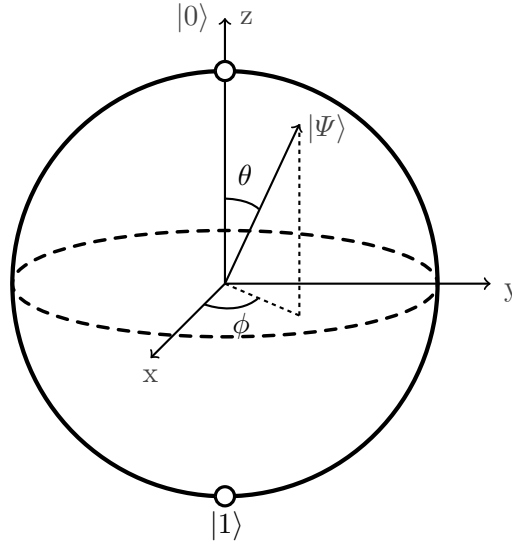


Figure 2.2: The representation of a two-level system with the Bloch-sphere. Any state $|\Psi\rangle$ lies on the surface of the Bloch-sphere defined by the two angles θ and ϕ .

2.1.2 Single qubit operations

When dealing with qubits, the first step towards quantum information toolkits are always operations changing the state of the qubit on the Bloch-sphere. These operations must preserve the norm of the state

$$|c_0|^2 + |c_1|^2 = 1, \quad (2.17)$$

and are thus described by 2×2 matrices (in the single qubit case).

The most important ones are the Pauli-matrices

$$X \equiv \begin{pmatrix} 0 & 1 \\ 1 & 0 \end{pmatrix}, Y \equiv \begin{pmatrix} 0 & -i \\ i & 0 \end{pmatrix}, Z \equiv \begin{pmatrix} 1 & 0 \\ 0 & -1 \end{pmatrix}, \quad (2.18)$$

which induce rotations of the state-vector around the respective axis.

These three gate-operations give rise to a very useful class of unitary operations when they are exponentiated, known as the rotation operators about the x , y and z axes,

which are given by [Nie00]:

$$\begin{aligned}
 R_x(\theta) &= e^{-i\theta X} = \begin{pmatrix} \cos\left(\frac{\theta}{2}\right) & -i \sin\left(\frac{\theta}{2}\right) \\ -i \sin\left(\frac{\theta}{2}\right) & \cos\left(\frac{\theta}{2}\right) \end{pmatrix} \\
 R_y(\theta) &= e^{-i\theta Y} = \begin{pmatrix} \cos\left(\frac{\theta}{2}\right) & -\sin\left(\frac{\theta}{2}\right) \\ \sin\left(\frac{\theta}{2}\right) & \cos\left(\frac{\theta}{2}\right) \end{pmatrix} \\
 R_z(\theta) &= e^{-i\theta Z} = \begin{pmatrix} e^{-\frac{\theta}{2}} & 0 \\ 0 & e^{\frac{\theta}{2}} \end{pmatrix}
 \end{aligned} \tag{2.19}$$

The rotations around the y - or x -axes (which one is arbitrary for now because the global phase does not matter, however see Sec. 4 for rotations around two axes at a time) are possible in our setup (in principle rotations around the z -axis are possible as well, but not used in the following experiments), by applying driving pulses with appropriate length and driving power as described in Sec. 2.1; θ becomes

$$\theta = \Omega_R t, \tag{2.20}$$

and thus inducing a phase-shift resulting in a e.g. $R_x(\pi/2)$ or a $R_x(\pi)$ rotation.

Note however, that a $R_x(2\pi)$ rotation induces a 180° global phase-shift, and only after a $R_x(4\pi)$ rotation the phase is back in its original state.

2.2 Structure of the NV-center

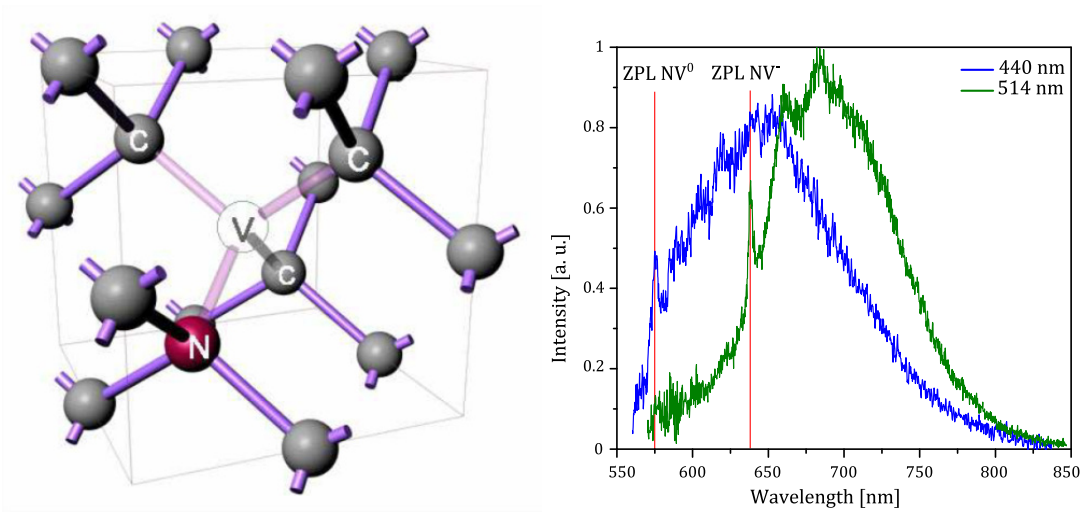
Amongst hundreds of point-defects in diamonds, the nitrogen-vacancy center is probably the best known one.

The center is formed by a substitutional nitrogen atom and an adjacent vacancy [Jel06], replacing two carbon atoms in the diamond lattice, with the nitrogen-to-vacancy axis pointing in the crystallographic [111] direction [Dav76]. This results in a C_{3V} symmetry, hence electronic states are characterized by how they transform under C_{3V} symmetry operations. This symmetry group consists of a three-fold rotational symmetry around the vertical symmetry axis (shown in Fig. 2.3a) and reflections in the three planes, containing the vertical symmetry axis and one of the nearest carbon sites [Chi06a].

The vacancy is surrounded by five dangling bonds, three electrons from the three adjacent carbon atoms, and two electrons from the nitrogen atom, forming electronic orbitals in the vacancy. This object is electrically neutral and thus called NV^0 . A sixth electron may bind to the NV center (possibly from other nitrogen impurities [Man06]) forming a negatively charged defect-center, known as NV^- .

Since the remainder of this thesis is mostly concerned with NV^- centers, the negative charge sign is omitted in the following.

The orbitals of the center are then filled according to Hund's rules. The first two



a Structure of the NV-center, showing the carbon lattice with the substitutional nitrogen atom, and an adjacent vacancy. The vertical symmetry axis is the N-V direction

b Fluorescence spectra of the NV^0 and NV^- -center at room temperature. Note that the excitation wavelengths were different, as indicated in the legend. One can see the two zero-phonon lines and the phonon sideband. The plots are normalized to cover the same area (plot taken from [Asl13])

Figure 2.3

orbitals ($1s$ and $2s$ -orbital in the case of an atom) are filled with four electrons leading to an overall orbital angular momentum of zero. The remaining two electrons are then left in orbits with non-zero angular momentum, and according to the second and third rule, the spin and orbital angular momentum become maximal.

Deriving the exact electronic structure is still a partially unsolved problem. Approaches have been made to solve this problem, with the best results given by the “linear combinations of atomic orbitals” (LCAO) approach [Doh10].

2.3 Spin properties of the NV-center and optical transitions

According to the LCAO approach the C_{3V} symmetry leads to possible orbits that can be calculated [Mes70]. The irreducible representations of this group correspond to the orbitals of the electrons:

1. 1A_1 is a spin and orbital singlet state, symmetric along the principle NV-axis. This state is a metastable state in the NV-center with a long lifetime of about 150 ns to 450 ns [Aco10]

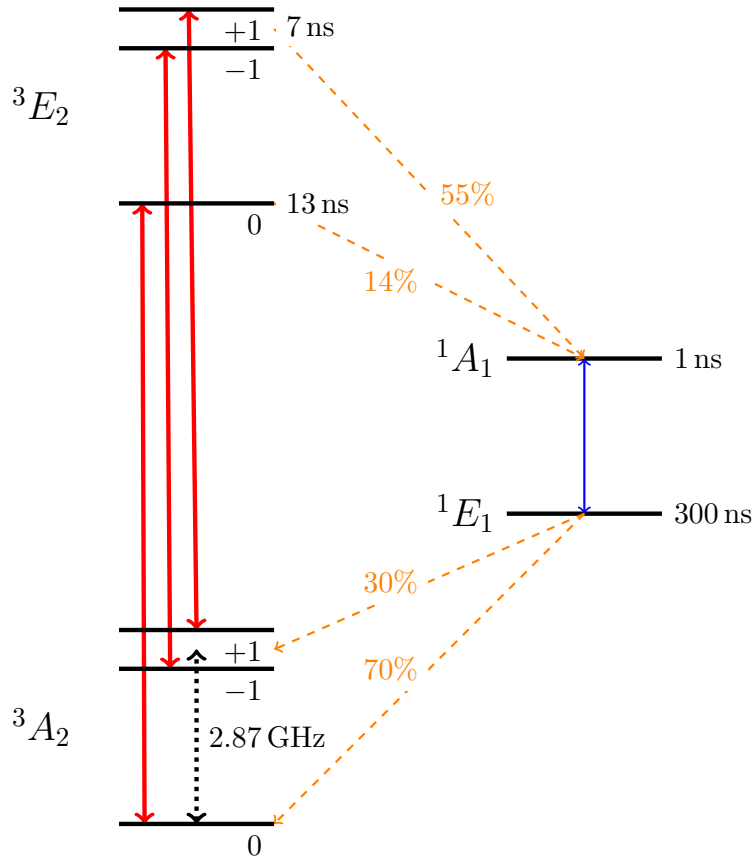


Figure 2.4: Term scheme of the NV-center at room temperature. Solid lines indicate allowed electric dipole transitions (red for the transitions we are interested in, and blue for a transition between the two metastable states), magnetic dipole transitions are shown as dotted black lines. Nonradiative intersystem crossing transitions are shown as dashed orange arrows. Level lifetimes and approximate branching ratios are depicted in the figure as well, taken from Ref. [Aco10]

2. 3A_2 is an orbitally non degenerate spin-triplet state, symmetric under rotation, which changes sign under reflection. This state is present in the NV-center as a spin-triplet ground state, split itself by spin-spin interactions (zero-field splitting), yielding one $m_s = 0$ with A character, and two $m_s = \pm 1$ states with E -character [Chi06b], split by 2.87 GHz (see Sec. 2.4 for the ground-state Hamiltonian)
3. 1E is a spin singlet, orbital degenerate doublet state. This state is an intermediate state in diamond, with a very short lifetime < 1 ns and thus not very important in further considerations [Aco10]
4. 3E is a spin triplet times orbital doublet state with twofold degeneracy. This state is the optically excited state in the NV center, with a lifetime of about 10 ns.

2.3.1 Optical transitions

According to Fermi's golden rule, electric dipole transitions between an initial state $|\Psi_i\rangle$ and a final state $|\Psi_f\rangle$ are allowed if their transition matrix element is non-zero:

$$\langle\Psi_i|\mathbf{d}\cdot\mathbf{E}|\Psi_f\rangle\neq 0, \quad (2.21)$$

with \mathbf{d} being the electrical dipole moment. This leads to the transitions depicted in Fig. 2.4 [Aco10].

At room temperature, where all of the following experiments were carried out, transitions between the optical ground- and excited state are spin-preserving, with the probability of a spin-flip ($\Delta m_s \pm 1$) being about 1% of the allowed transition rates [Ste09]. Thus three prominent transitions are present between the ground and excited triplet-states, with a transition wavelength of 637 nm, known as the zero-phonon line (ZPL), and one transitions between the two singlet levels with 1042 nm (the zero phonon line for the NV⁰ is at 575 nm). In addition there are non-radiative transitions, depicted as dashed arrows in Fig. 2.4 [Aco10].

2.3.1.1 Coupling to phonons

The NV defect not only couples to photons, but also quite strongly to local or global vibrations in the crystal (phonons). In fluorescence, this has the (somewhat inconvenient) effect that not all the fluorescence intensity is found in the 637 nm ZPL, but most of it in the phonon sideband [Nb13a] (see Fig. 2.3b). This is also the reason why off-resonant excitation at wavelengths shorter than the ZPL is possible, exciting the center to its optically excited state plus phonons, which then decays rapidly and non-radiatively to the excited states. The advantage of exciting into the phonon-sideband versus an excitation at 637 nm is the fact that it is not necessary to monitor the exact wavelength of the excitation laser, since inaccuracies of several nanometers do not matter.

2.3.1.2 Fluorescence time traces and spin polarization

As stated in the previous section, optical transitions between the triplet ³A state and the triplet excited state ³E are spin conserving; with resonant excitation (637 nm) spin-flips for the $m_s = 0$ transition occur with a probability of roughly one percent. However spin-flips can occur via the so called inter-system crossing (ISC) process. As depicted in Fig. 2.4 the $m_s = \pm 1$ spin states preferably undergo a non-radiative transition to the two singlet states, with the lower one being a metastable state with a lifetime of ≈ 300 ns. While the spin is trapped in the relatively long-living metastable state, it cannot undergo additional optical cycles, and remains dark, until the ¹A state decays, preferably to the $m_s = 0$ ground state. Since this ISC mainly occurs for the excited $m_s = \pm 1$ states, the spins get optically pumped into the $m_s = 0$ ground state, resulting in a higher fluorescence. Hence the $m_s = 0$ state is called the "bright" state, whereas

the $m_s = \pm 1$ states are called “dark” states. This ISC hence gives an easy way to optically read out the state of the spin.

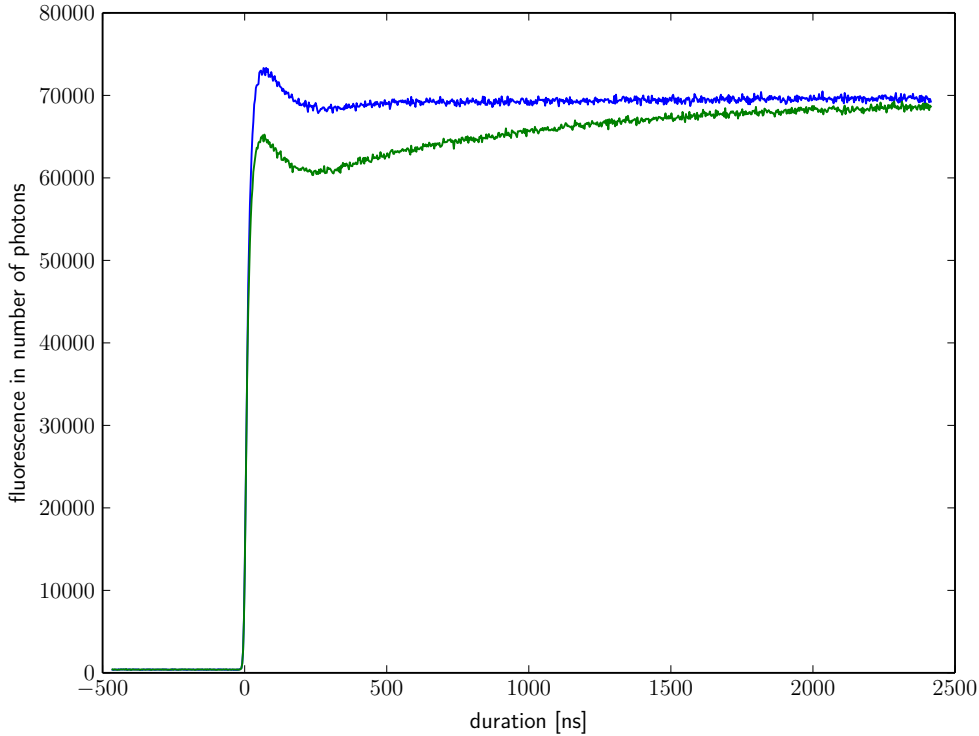


Figure 2.5: Fluorescence time traces under constant illumination showing the difference in fluorescence for the bright and dark state. The blue trajectory shows the $m_s = 0$ state, whereas the green trajectory the $m_s \pm 1$ state. These curves are recorded after integrating over a lot of sweeps in order to reduce shot-noise and get rather smooth data curves.

Distinguishing between the two states of the spin is done by measuring the fluorescence time traces under constant illumination. Starting in the $m_s = 0$ state, an intensity peak immediately after the illumination is detectable, decaying to equilibrium within approximately one microsecond. Starting in the $m_s = \pm 1$ state the fluorescence trace looks different, showing a sharp drop of about 30% below the equilibrium level. This dip occurs due to the aforementioned metastable state that does not fluoresce, but decays after 300 ns. Thus both fluorescence time traces return to equilibrium after a few microseconds. By integrating over a lot of sweeps, in order to get smooth fluorescence data time traces, it is then possible to determine the state of the spin by comparing the initial fluorescence to the fluorescence in the steady state. The time traces for both cases are shown in Fig. 2.5.

By off-resonant optical pumping these spin dynamics provide a method to initialize

the spin, since the $m_s = \pm 1$ states tend to get transformed to the $m_s = 0$ state after a few optical cycles with a polarization probability $> 80\%$ after $3 \mu\text{s}$ of optical excitation. This is used for optically detected magnetic resonance as well as pulsed measurements described in Sec. 3.2.5.

2.4 Fine- and hyperfine structure and transitions in the ground-state

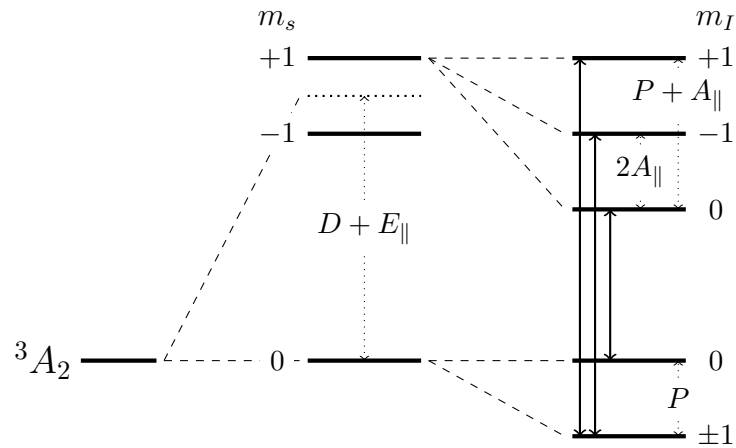


Figure 2.6: Term scheme of the NV-ground state fine- and hyperfine structure, due to the nuclear spin of the adjacent ^{14}N atom. An external magnetic field lifts the degeneracy of the $m_s = \pm 1$ states. Solid lines indicate allowed magnetic dipole transitions.

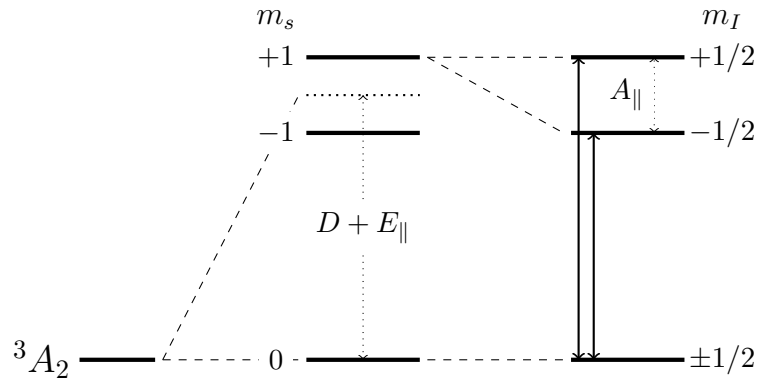


Figure 2.7: Term scheme of the NV-ground state fine- and hyperfine structure, due to the nuclear spin of the adjacent ^{13}C atom. An external magnetic field lifts the degeneracy of the $m_s = \pm 1$ states. Solid lines indicate allowed magnetic dipole transitions. A_{\parallel} can be up to 130 MHz for very close ^{13}C atoms.

Since the qubit levels used in the experiments throughout this thesis were not the optical ground- and excited states, but the spin sublevels of the optical ground state,

the fine- and hyperfine structure of the ground state play an important role in further considerations. These states are well suited for quantum information processing, because information stored in this system has a surprisingly long coherence time, due to the high Debye temperature in diamond and hence very few populated phonon modes at room temperature [Alb13]. Furthermore, in contrast to optical transitions, spins do not couple strongly to these bulk phonons. Dephasing is therefore usually not limited by coupling to phonons in the diamond, but coupling to other spins in the surrounding spin bath (see Sec. 3.2.3)

Without external fields one can observe a lift of the degeneracy of the $m_s = 0$ and $m_s \pm 1$ states, due to a dipole-dipole interaction of the two unpaired electron spins in the optical ground state as well as in the optical excited state. Additional to this zero-field splitting (H_{ZFS}), the C_{3V} symmetry of the center is slightly broken by a non-axial strain field created by irregularities in the surrounding crystal lattice (crystal field) lifting the degeneracy of the $m_s = -1$ and $m_s = +1$ states. One of the transitions from $m_s = 0$ to either $m_s = +1$ or $m_s = -1$ is then our desired qubit state used to store quantum information.

The electron spin however couples also to the nuclear spin of the adjacent nitrogen atom (mainly ^{14}N , see Fig. 2.6) and possibly to the nuclear spin of a ^{13}C atom (natural abundance of 1.1% [Sme11], see Fig. 2.7) in the neighboring lattice sites, as well as to external or internal electrical and magnetic fields (i.e. Stark- and Zeeman-shift).

The Hamiltonian taking into account the fine and hyperfine-splitting with coupling to a ^{14}N and a ^{13}C nuclear spin is given by [Sme11]:

$$\begin{aligned}
H_{GS} &= H_{ZFS} + H_{Zeeman} \\
&\quad + H_{HF}^N + H_{HF}^C + H_{nucl.quadrupole}^N + H_{nucl.Zeeman}^N + H_{nucl.Zeeman}^C \\
&= D \left[S_z^2 - \frac{1}{3} \mathbf{S} \cdot (\mathbf{S} + 1) \right] + \mu_B g_e \mathbf{S} \cdot \mathbf{B} \\
&\quad + A_{\parallel}^N S_z I_z^N + A_{\perp}^N (S_x I_x^N + S_y I_y^N) + A_{\parallel}^C S_z I_z^C + A_{\perp}^C (S_x I_x^C + S_y I_y^C) \\
&\quad + P \left[I_z^{N^2} - \frac{1}{3} \mathbf{I}^N \cdot (\mathbf{I}^N + 1) \right] + \mu_B g_N \mathbf{I}^N \cdot \mathbf{B} + \mu_B g_C \mathbf{I}^C \cdot \mathbf{B}
\end{aligned} \tag{2.22}$$

with a strong quadrupole coupling of $P \simeq 5$ MHz, splitting the $m_N = 0$ state and the $m_N = \pm 1$ state [Chi06a]. Interactions between the nitrogen nuclear spin, and the electron spin are given by an axial and transversal term, $A_{\parallel}^N = 2.3$ MHz and $A_{\perp}^N = 2.1$ MHz [Jel06], whereas the coupling of the nuclear ^{13}C spin to the electron spin ($A_{\parallel}^C, A_{\perp}^C$), depends on the position of the carbon atom with respect to the nitrogen-vacancy center, and can range from 126 MHz for a nearest-neighbor ^{13}C nucleus to a few MHz for nuclei further away [Sme11]. g, g_N and g_C are the respective gyromagnetic ratios.

The quantization axis points directly along the NV-axis as long as non-axial effects

(especially strong non-axial magnetic fields) do not become too large.

The Zeeman effect is often used to lift the degeneracy of the $m_s = \pm 1$ states, with 2.8 MHz/G, by applying a magnetic field preferably along the NV axis. The Stark-effect is several orders of magnitude smaller and can usually be neglected (not included in the above Hamiltonian), nevertheless experiments have been done using its effect to sense electrical fields [Dol11].

NV-centers formed with ^{15}N instead of ^{14}N are possible as well, which results in a slightly different Hamiltonian because of the spin 1/2 character of the ^{15}N nucleus.

3 Experimental setup and measurement schemes

3.1 Confocal microscope

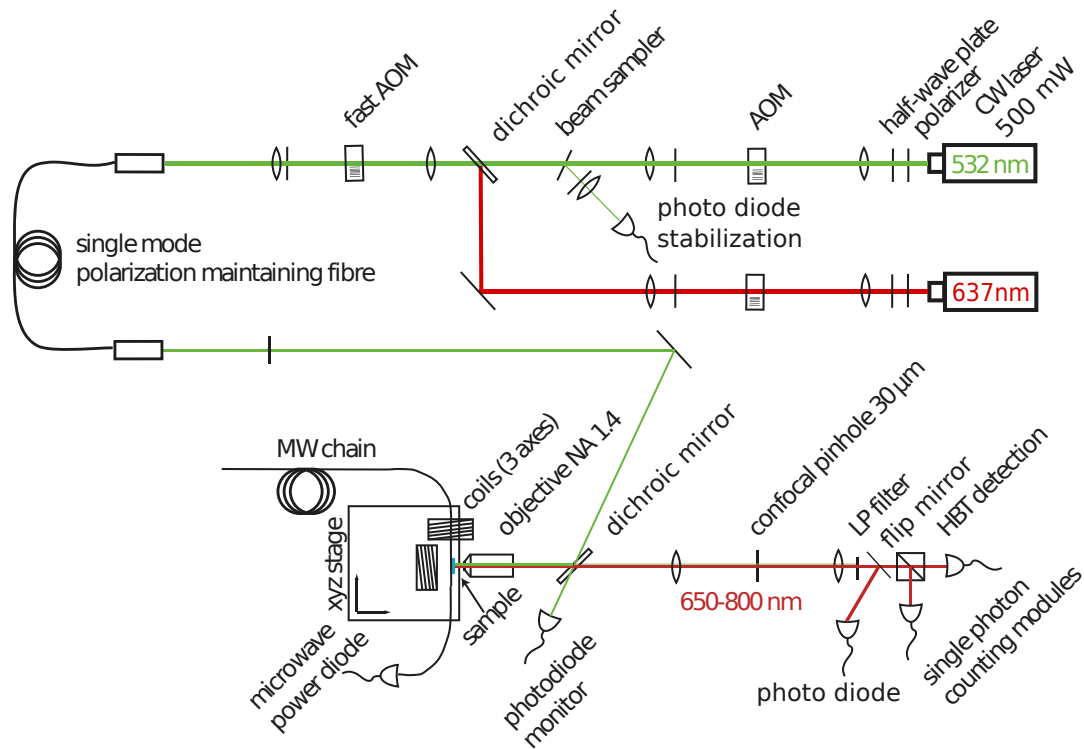


Figure 3.1

An overview of the optical setup is given in Fig. 3.1, which shows a sketch of the included devices. This confocal microscope with laser excitation and single-photon fluorescence detection was already finished at the start of this thesis, thus the following section gives only a short overview outlining the basic ideas. For more detailed information, the reader is referred to Ref. [Nb13a].

First a frequency doubled solid state laser provides ≈ 500 mW of green 532 nm excitation light, which is stabilized using an acousto-optic modulator (AOM) via a feedback loop, where a few percent of the laser-beam are picked off the first diffraction order generated by the AOM and focused onto a photo diode. During this thesis a laser diode

was installed which provides red 637 nm light (≈ 300 mW) to resonantly excite the NV-center. Another AOM stabilizes and regulates the intensity of that second laser. The red and/or the green light is then merged in one beamline by using a dichroic mirror, transparent for the green beam, but reflecting for the red one.

The beam is then focused onto a second AOM, optimized for fast switching, which can be used to chop the laser, generating laser pulses with a few nanoseconds rise- and fall-time. The beam is then coupled into a single mode polarization maintaining fiber, which serves a dual purpose: On the one hand to clean up the beam profile, because only a lowest order Gaussian beam is transmitted, and on the other hand to separate the quite sensitive beam preparation part from the microscopy stage.

After the fiber a second dichroic mirror is used to reflect the incoming laser beam (red and/or green) onto the sample. The scattered light from the NV-center follows the same path in the opposite direction, and since the dichroic mirror is transparent for light with a wavelength greater than 658 nm most of this light is then focused onto a pinhole and an additional 650 nm long-wavelength-pass filter, to filter out most of the undesired NV⁰ fluorescence. Finally two avalanche photodiodes (APDs) detect the fluorescence photons. The pulses generated by the APDs are registered by a very fast time-to-digital converter card and uploaded to the control PC.

The objective focusing the incoming light onto the sample and at the same time collecting the scattered light from the sample (Olympus PLAPON 60XO, apochromat, NA 1.42, working distance 150 μ m, spring loaded) has a very high numerical aperture, in order to collect as many photons as possible. Moreover immersion oil between the sample and the objective is used, in order to reduce the angle of total internal reflection at the transition from diamond to the oil by more closely matching the refractive index of diamond (diamond $n = 2.4$, oil $n = 1.4$, air $n = 1.0$)

3.2 Electron spin resonance experiments

3.2.1 Microwave chain

For driving the transition at 2.87 GHz and conducting experiments regarding spin-manipulation, a microwave signal at the sample with appropriate power is needed. Furthermore shaping of the pulses (see Sec. 4) and fast chopping for pulsed measurements (3.2.5) is required. For this purpose several microwave (MW) devices are necessary, which will be discussed in the following.

The main carrier signal is provided by a signal generator (Anritsu 3691B) operating in a frequency range from 2 GHz to 10 GHz with a maximum power output of 30 dBm (up to 20 dBm the output is leveled). The signal generator is usually operated at the resonance frequency (e.g. 2.87 GHz), with a signal that can be chopped using a fast microwave switch. For fast switching to a second signal at a different frequency (see Sec. 4.3.2 below), a second signal generator (Thurlby Thandar TGR6000) and a second microwave switch, which switches from one source to the other one is used. This second

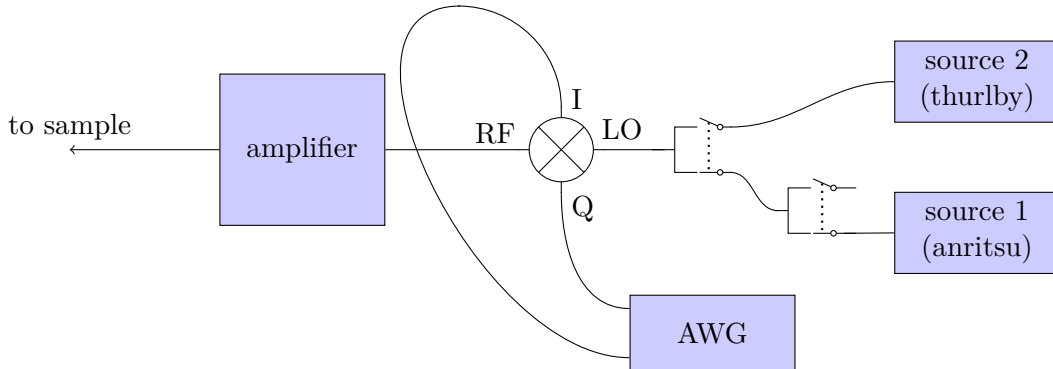


Figure 3.2: The microwave chain, providing the 2.87 GHz signal. Two switches multiplex two different sources and chop the signal. The IQ mixer modulates two baseband signals from the arbitrary-waveform generator onto the microwave carrier. The amplifier then amplifies this quadrature-modulated signal.

signal generator operates in a frequency range from 10 MHz to 6 GHz, with a maximum output power of 7 dBm. The mixer has its optimal working point at 13 dBm (for the desired frequency range), thus the input at the local oscillator (LO) port has to be at this power, making it necessary to use a small microwave amplifier amplifying the signal from the second generator to the required 13 dBm.

The carrier signal is then fed into the LO-input of an IQ-mixer (Marki Microwave IQ LMP1545) mixing two channels from a homemade arbitrary-waveform generator (AWG with a Spartan-6 FPGA) onto the carrier signal. The AWG is able to generate signals with a temporal resolution of 5 ns and a rise- and fall-time within the same magnitude. The quadrature modulated RF-signal is then fed into a microwave amplifier ZHL-16W-43+, amplifying the signal by 45 dB. The amplified signal is sent to the diamond sample (for more information about the sample and sample-holder see Ref. [Kow13]). The sketch of this chain showing the main included devices is illustrated in Fig. 3.2.

3.2.2 Coils

For almost all of the following experiments, a two-level system (apart from the hyperfine-splitting) was needed, and therefore the degeneracy of the $m_s = \pm 1$ states needed to get lifted. Using the Zeeman effect one can easily get rid of the $m_s = -1$ state by applying an appropriate magnetic field (preferably along the NV-axis) of several tens of Gauss, lifting the degeneracy, and using the $m_s = 0$ and $m_s = 1$ levels as the qubit states. Since the confocal volume is rather small and hence the requirements on magnetic field homogeneity are easy to meet, three coils (as opposed to three Helmholtz pairs) are sufficient. Each coil can be controlled using a separate power supply.

For stronger fields, which are sometimes needed, a permanent magnet is used to provide $\simeq 100$ G of magnetic field (in comparison the coils are able to provide $\simeq 15$ G).

Aligning the magnetic field of the permanent magnet along the NV-axis can be very tedious, therefore using the electromagnets was generally preferred when possible.

3.2.3 Dephasing and loss of coherence

All considerations in Sec. 2.1, have been carried out using unitary dynamics. In reality however non-unitary dynamics like spontaneous emission in the excited state and also small phase-shifts due to a slightly different magnetic environment for each qubit, play an important role in all following considerations.

These processes are described by three different time constants, T_1 for the spontaneous emission (sometimes called longitudinal relaxation), T_2 for spin-spin relaxation (sometimes called transversal relaxation), and T_2^* for inhomogeneous broadening [Fox06].

- The T_1 (longitudinal) decoherence process is probably the simplest to understand, and occurs because the excited state in every qubit has a tendency to decay to the ground state due to spontaneous emission, interactions with phonons or other spin-flipping process. This decay process occurs stochastically and thus randomly brakes the coherence of the wave function. T_1 ranges from ns for optical transitions to many minutes in NMR.

- The transversal dephasing process is more subtle to understand.

T_2 is the time constant describing homogeneous broadening, more commonly referred to as spin-spin relaxation in NMR. In some sense T_2 is intrinsic to the qubit and its local spin environment. The spins couple to this environment and lose coherence, on a timescale given by T_2 . In the case of a single qubit this dephasing process describes the loss of the phase relation between the two basis states in a superposition state. T_2 is typically measured using a spin-echo sequence as described in Sec. 3.2.5.3, where the time-constant defining the decay of the envelope corresponds to T_2 .

- When considering ensembles of spins, the phase relations between individual qubits can get lost due to their slightly different intrinsic resonance frequencies (inhomogeneous broadening), or extrinsic sources of spectral drift, such as inhomogeneities of the magnetic field in NMR. This happens on a timescale of T_2^* and results in an inhomogeneous broadening of the resonance lines.

In the context of a single qubit, the notion of T_2^* has to be redefined in order to make sense: Here, T_2^* refers to the timescale of a dephasing that is reversible (e.g. by inverting the system, or the bath), and T_2 to the timescale of a dephasing that is not reversible in a given experimental context.

Measuring T_2^* is typically done using two different methods: The first one is described in more detail in Sec. 3.2.5.2 using a Ramsey-type measurement and

extract the time constant describing the decay of the envelope. An alternative method is to record ODMR-spectra with decreasing power and use these measurements to linearly extrapolate the linewidth at zero MW power. T_2^* is then given by the FWHM at zero MW-power according to

$$T_2^* = \frac{1}{\pi\Gamma_{FWHM}}. \quad (3.1)$$

In the case of NV-centers, T_1 is very long (seconds at room temperature) due to a long excited state lifetime and weak coupling to spin-flipping phonon-mediated processes (note that this is, up to some extent, true for single NV centers as well as ensembles of NV centers) [Pha13].

T_2 and T_2^* however vary strongly from sample to sample, and is different for (dense) ensembles and single NV-centers:

- single NV in chemically pure diamond (with natural 1.1% abundant ^{13}C atoms): The dephasing is limited by the dipolar hyperfine coupling to the ^{13}C spin bath [Pha13].
- single NV in isotopically pure diamond: The dephasing is limited by external magnetic noise, which results in very long T_2 and T_2^*
- low-density ensembles of NVs in a nitrogen-rich diamond: The limiting bath are impurities from other spins (P_1 centers), which dominates the dephasing
- high-density ensembles of NVs: coupling between NVs may become dominant, reducing T_2 and T_2^* drastically.

3.2.4 ODMR

The difference in fluorescence for the $m_s = 0$ and $m_s = \pm 1$ states, as derived in Sec. 2.3 gives the opportunity to perform optically detected magnetic resonance (ODMR). A MW signal of constant power is applied (via one of the two IQ channels of the AWG). While continuously exciting and counting fluorescence, the frequency of the MW signal is scanned across a relevant frequency range, lasting a few milliseconds at each step. Averaging over several sweeps, one can then detect dips of the fluorescence rate at certain MW frequencies, which correspond to spin resonance transitions.

By reducing the microwave power and hence the power broadening of the resonance lines (see Ref. [Vit01]), fine and hyperfine-transitions are detectable (see Fig. 3.3 with greater detail in the caption).

The ODMR-technique is crucial for determining the exact resonance frequency of a transition, important for almost all of our measurements (see Sec. 4.3.2 as an example), and/or determining the spectral linewidth of inhomogeneously broadened spin-ensembles.

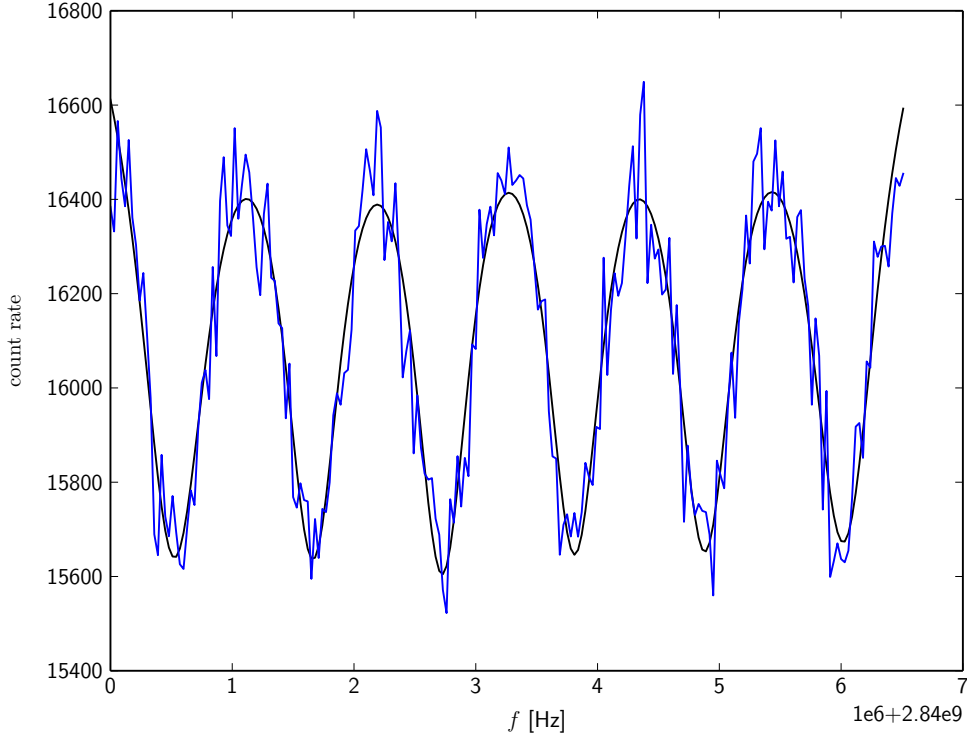
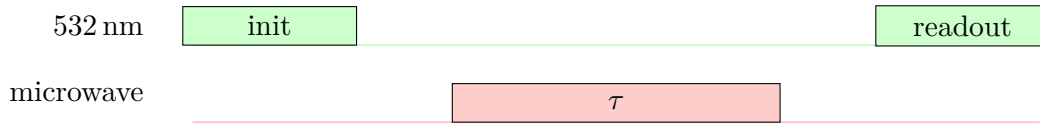


Figure 3.3: Hyperfine-resolved ODMR spectrum of the $m_s = -1$ to $m_s = 0$ transition of a single NV center. The hyperfine structure occurs due to coupling to an adjacent ^{14}N and one nearby ^{13}C nuclear spin. The six lines are fitted with 6 Lorentzians, giving the exact positions of the transition frequencies.

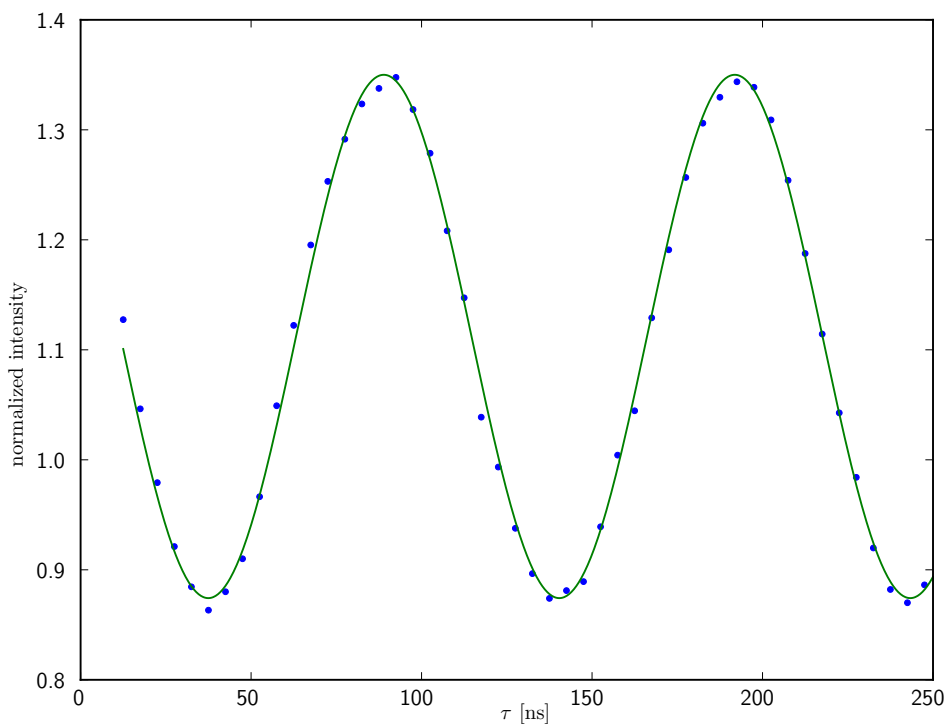
3.2.5 Pulsed measurements

Having obtained the exact transition frequencies from ODMR measurements, the next step is to coherently manipulate the spin. This is achieved by initializing the spin in the $m_s = 0$ state, by shining in the excitation laser for about $3\ \mu\text{s}$ and waiting for another microsecond in order to let the metastable state decay to the optical ground state. Afterwards different pulse sequences are applied (depending on the experiment) and finally the spin state is read out, by using the excitation laser once more, and counting fluorescence photons. This procedure is repeated several million times to get smooth fluorescence time traces. By scanning different parameters in such a measurement like the duration of the microwave pulse, one can then observe different behaviors like for example Rabi-oscillations, as discussed in the following section.

3.2.5.1 Rabi nutations



a Measurement scheme for Rabi-oscillations. Oscillations are recorded by scanning the length of the microwave pulse τ



b Simple Rabi-nutations for a single spin. The blue data points are fitted with a sine (green curve). The appropriate $\pi/2$ -, π -times are then taken from this fit.

Figure 3.4

As derived in Sec. 2.1, a population transfer of a (single) spin is achieved by shining in (resonant) electromagnetic radiation for a certain amount of time. The rate at which the spins are rotated depends on the power of the driving field and its detuning. By scanning the duration τ of the applied driving field, the period of these so called Rabi-oscillation is obtained as well as the time needed to flip the spin (π -pulse) or to drive it into an equal superposition of $|0\rangle$ and $|1\rangle$ (i.e. $\pi/2$ -pulse).

The experimental sequence is sketched in Fig. 3.4a, and the resulting Rabi-nutations are shown in Fig. 3.4b. Since dephasing processes limit the maximum duration of coherent manipulation experiments, high MW amplitudes are needed in order to drive fast enough Rabi rotations. Therefore one of my predecessors, Adrian Kowar [Kow13], developed gold structures on the sample in the course of his Master’s thesis. This allows to get higher MW powers at the place of the NV-centers, resulting in Rabi-oscillations at rates as fast as ≈ 50 MHz. With a gold-wire above the sample, one can achieve ≈ 10 MHz Rabi-oscillations.

Since the spin resonance transitions show hyperfine structure, we are generally not working with single spins, and interactions of several detuned spins with the driving field always occur. This leads to beating of the Rabi-oscillations, when working with a single NV-center. By working with ensembles of inhomogeneously broadened ensembles of spins, the different frequencies of the spins average out, and beatings are usually no longer observable.

3.2.5.2 Free induction decay measurements

Another basic measurement scheme is the so called free induction decay (or Ramsey-) measurement. As described in Sec. 3.2.3 the free induction decay time T_2^* can be measured using this technique. First the spin is initialized in the $m_s = 0$ state with the standard procedure. Then a $\pi/2$ -pulse is applied, creating a superposition $|\Psi\rangle = \frac{1}{\sqrt{2}}(|0\rangle + |1\rangle)$. The system is left to evolve freely during a period τ , during which the spin may pick up a certain amount of phase, either due to interactions with the surrounding magnetic moments (spin-bath) or inhomogeneous broadening (see Sec. 3.2.3).

Without the dephasing environment the signal would oscillate at a frequency corresponding to the detuning of the microwave signal, because a phase shift $\Delta\Phi \propto \Delta\omega\tau$ proportional to the free precession time τ and the detuning of the driving field is induced. This is therefore a good way to see the effect of different resonance frequencies occurring due to the hyperfine-splitting, resulting in a beating of the respective oscillations. Fig. 3.5b shows this behavior, with frequencies corresponding to the ± 2.2 MHz detuned spins (and additional ^{13}C transitions), which are fitted using 6 sinusoidal curves using the transition frequencies derived in Sec. 2.4.

Using an ensemble of spins and not a single spin, one can experience a similar effect. The fact that the resonance frequencies of the spins in an ensemble are slightly different (inhomogeneous broadening) leads to a decay of the FID-signal, although beating of the individual resonance frequencies is no longer observed because the large amount of different frequencies average out.

3.2.5.3 Spin-echo measurements

The effects of dephasing due to a static set of detunings or a slowly varying bath (as characterized by the in the T_2^* parameter) can be reversed by employing a so-called

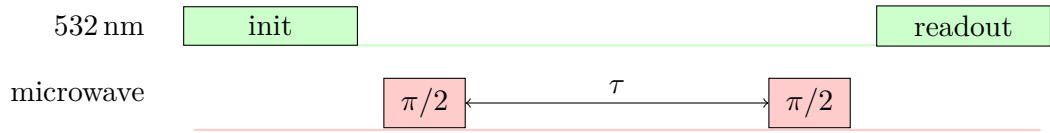
spin echo (sometimes called Hahn echo) sequence:

This measurement is the simplest way to recover coherence from the bath, and is achieved by a $\pi/2 - \tau - \pi - \tau - \pi/2$ sequence (more details in Fig. 3.6a). Instead of generating a superposition state and reading it out again after a free precession time like in the FID-measurement, a π -pulse in the middle of two equally long free precession-times τ is introduced, leading to a refocusing of the information from the bath onto the center spin (if the bath has a coherence time longer than the system, i.e. a non-Markovian bath). Noise components slower than 2τ get canceled out, leading to a longer coherence time known as T_2 limited by “intrinsic” dephasing and in most of the cases longer than T_2^* (see Sec. 3.2.3).

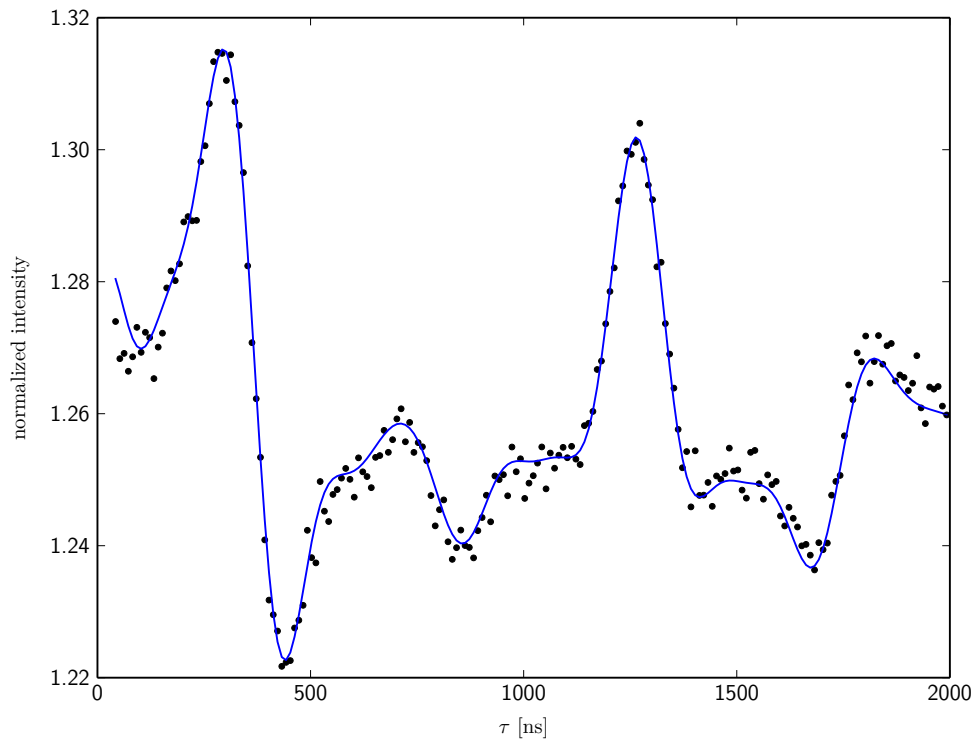
The exact sequence and the measurement results are shown in Fig. 3.6a. Revivals which can be seen in the experimental data (at $\simeq 80\,000$ ns in Fig. 3.6b), occur because of the limiting surrounding ^{13}C spin bath. If the free precession time τ matches the Larmor-frequency of the surrounding ^{13}C spins, the phase shifts during the de- and rephasing intervals cancel out. The height of the peaks itself however decreases, since the decoherence time of the bath itself is limited. By isotopically purifying the diamond, and getting rid of limiting ^{13}C nuclei, T_2 times up to the millisecond range are possible.

These results for a single NV-case, cannot be reconstructed using ensembles of NV-centers, as the electron-spin bath from substitutional nitrogen-atoms dominates. This leads to a decrease of the T_2 time, and T_2 is in most cases not significantly larger than T_2^* anymore, but on the same order of magnitude.

Moreover, revivals can no longer be observed, since the dephasing environment is now dominated by a nitrogen-spin bath instead of coupling to the ^{13}C bath: electron spins interact much more strongly with each other and the environment than nuclear spins and hence lose their coherence more quickly. Experimental data for that case can be found in Sec. 4.4.2.

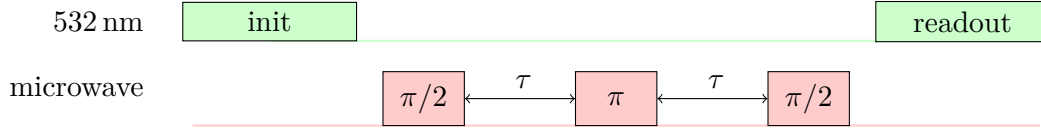


a Measurement scheme for FID-measurement. Oscillations are recorded by scanning the free precession time τ

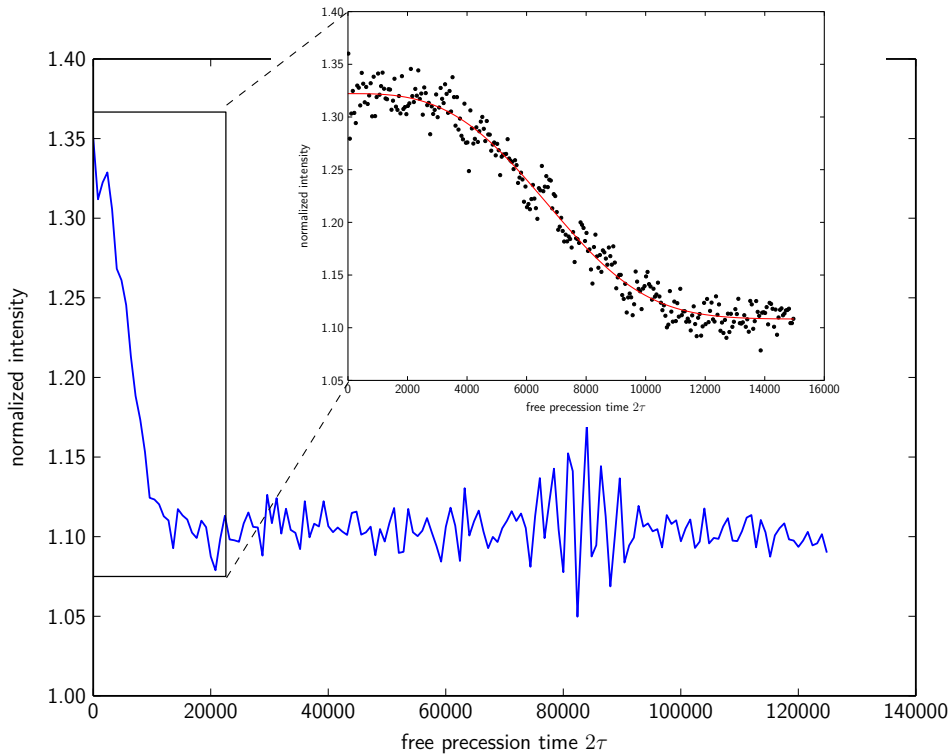


b Free induction decay measurement for 6 detuned spins (for spectrum see Fig. 3.3). The experimental data (black dots) was fitted using the method described in Ref. [Xin12], indicating a T_2^* time of 1536 ns for this NV-center

Figure 3.5



a Measurement scheme for spin-echo-measurement. By scanning the free precession time τ , the typical spin-echo behavior is obtained



b Spin-echo measurement for a single NV-center. One (faint) ^{13}C revival can be seen at $\simeq 80\,000$ ns. The inset shows the time-behavior of the first oscillation, fitted according to Ref. [Sta10]. The initial spin echo decays on the timescale T_2^* , while the envelope of the ^{13}C revivals, yields the T_2 time (not fitted in this figure, because of the small number of revivals), about 50-100 times longer than T_2^* in the case of a single NV in chemically ultra-pure diamond.

Figure 3.6

4 Implementing smooth optimal control

In order to facilitate applications of NV centers in quantum computing and nanoscale sensing, robust and high-fidelity control of their spin degree of freedom is a crucial requirement.

One way to do this is to use optimal control techniques, developed in the mid-20th century, mainly for robust NMR sequences, but also suitable for our qubit system.

The following section aims to do exactly this, by showing how to implement a new and promising set of optimal control pulses, named Smooth Optimal Control and developed by our collaborators Dr. Florian Mintert and colleagues at the Freiburg Institute for Advanced Studies (FRIAS). After the implementation and verification of these pulses, as a final result magnetometry using this Smooth Optimal Control pulses has been done showing improved sensitivity compared to less robust control techniques.

4.1 Theory

Since the theoretical approach to the method described here, is not the subject of this thesis, the following theoretical description covers only the basic ideas behind the Smooth Optimal Control technique. For more detailed explanations see Ref. [Bar13] and Ref. [Nb13a].

The basic idea behind every optimal control technique is to minimize (or maximize) a performance measure (e.g. fidelity etc.) by tuning different controls under given physical constraints. More formally this means, that we need to find a control vector $\mathbf{u}^*(t)$ which causes the system

$$\dot{\mathbf{x}}(t) = \mathbf{a}(\mathbf{x}(t), \mathbf{u}(t), t) \quad (4.1)$$

to follow an admissible (i.e. satisfying given constraints) trajectory $\mathbf{x}^*(t)$ that minimizes/maximizes a performance measure

$$\mathbf{J} = h(\mathbf{x}(t_f), t_f) + \int_{t_0}^{t_f} g(\mathbf{x}(t), \mathbf{u}(t), t) dt, \quad (4.2)$$

with h and g as scalar functions, and t_0 and t_f as initial and final time [Kir70].

The system we want to apply this optimal control algorithm to is given by a magnetic moment (i.e. our NV-electron) in an oscillating magnetic field (i.e. our microwave-

signal). The Hamiltonian describing this approximate two-level system, is given by

$$\hat{H} = -\boldsymbol{\mu} \cdot \mathbf{B} = \frac{1}{2} \hbar \gamma \boldsymbol{\sigma} \cdot \mathbf{B} \quad (4.3)$$

with γ being the gyromagnetic ratio, $\hat{\sigma}_i$ the Pauli-matrices and $\boldsymbol{\mu}$ the magnetic dipole moment. The zero-field-splitting of 2.87 GHz plus an applied static magnetic field induces a constant effective B_0 -field pointing in z -direction (our quantization axis), while the microwave signal adds a time dependent field chosen to be linearly polarized in x -direction (the global phase is unimportant). Taking this into account leads to

$$\hat{H} = \hat{H}_D + \hat{H}_C(t) = \frac{\hbar \omega_0}{2} \hat{\sigma}_z + \frac{1}{2} \hbar \gamma \hat{\sigma}_x (I(t) \cos(\omega_0 t) - Q(t) \sin(\omega_0 t)), \quad (4.4)$$

where $\omega_0 = \gamma B_0$ is the Larmor-frequency. \hat{H}_D is the system Hamiltonian with no adjustable components (inducing a precession around the applied constant magnetic field with the Larmor-frequency). The time-dependent part $\hat{H}_C(t)$ of the Hamiltonian contains the oscillating magnetic driving fields that we apply to the spin using an arbitrary wave generator, mixer and amplifier. This is the time dependent adjustable control Hamiltonian, where $I(t)$ and $Q(t)$ are the only directly adjustable parameters.

In order to simplify this Hamiltonian, we need to look at wavefunctions in the rotating frame

$$|\Psi'(t)\rangle = e^{i\omega_0 \hat{\sigma}_z t/2} |\Psi(t)\rangle. \quad (4.5)$$

This state can be evolved in time, using Schrödinger's equation (with some algebraic simplifications)

$$\begin{aligned} i\hbar \frac{d}{dt} |\Psi'(t)\rangle &= \left(-\frac{\hbar \omega_0 \hat{\sigma}_z}{2} + e^{i\omega_0 \hat{\sigma}_z t/2} \hat{H}(t) e^{-i\omega_0 \hat{\sigma}_z t/2} \right) |\Psi'(t)\rangle \\ &= \hat{H}'(t) |\Psi'(t)\rangle, \end{aligned} \quad (4.6)$$

yielding the Hamiltonian in the rotating frame

$$\hat{H}'(t) = \left(-\frac{\hbar \omega_0 \hat{\sigma}_z}{2} + e^{i\omega_0 \hat{\sigma}_z t/2} \hat{H}(t) e^{-i\omega_0 \hat{\sigma}_z t/2} \right). \quad (4.7)$$

Focusing now on the last term, and inserting the Hamiltonian from Eq. 4.4 one gets:

$$\begin{aligned} e^{i\omega_0 \hat{\sigma}_z t/2} \hat{H}(t) e^{-i\omega_0 \hat{\sigma}_z t/2} &= \\ \frac{\hbar}{2} (\omega_0 \hat{\sigma}_z + \gamma e^{i\omega_0 \hat{\sigma}_z t/2} (I(t) \cos(\omega_0 t) - Q(t) \sin(\omega_0 t)) \hat{\sigma}_x e^{-i\omega_0 \hat{\sigma}_z t/2}) & \end{aligned} \quad (4.8)$$

The field may now be rewritten as two counter-rotating waves:

$$\cos(\omega_0 t) \hat{\sigma}_x = \frac{1}{2} (e^{i\omega_0 t} (\hat{\sigma}_+ + \hat{\sigma}_-) + e^{-i\omega_0 t} (\hat{\sigma}_+ + \hat{\sigma}_-)) \quad (4.9)$$

$$\sin(\omega_0 t) \hat{\sigma}_x = \frac{1}{2i} (e^{i\omega_0 t} (\hat{\sigma}_+ + \hat{\sigma}_-) - e^{-i\omega_0 t} (\hat{\sigma}_+ + \hat{\sigma}_-)), \quad (4.10)$$

with $\hat{\sigma}_\pm = (\hat{\sigma}_x \pm i\hat{\sigma}_y)/2$.

Thus,

$$\begin{aligned} H'(t) &= -\frac{\hbar\omega_0}{2} \hat{\sigma}_z + \frac{\hbar}{2} (\omega_0 \hat{\sigma}_z + \gamma e^{i\omega_0 \hat{\sigma}_z t/2} (I(t) \cos(\omega_0 t) - Q(t) \sin(\omega_0 t)) \hat{\sigma}_x e^{-i\omega_0 \hat{\sigma}_z t/2} \\ &= \frac{\hbar\gamma}{2} (I(t) ((\hat{\sigma}_+ + \hat{\sigma}_-) + (e^{2i\omega_0 t} \hat{\sigma}_+ + e^{-2i\omega_0 t} \hat{\sigma}_-)) \\ &\quad - \frac{Q(t)}{i} ((\hat{\sigma}_- - \hat{\sigma}_+) + (e^{2i\omega_0 t} \hat{\sigma}_+ - e^{-2i\omega_0 t} \hat{\sigma}_-))). \end{aligned} \quad (4.11)$$

Using the rotating wave approximation (same argumentation as in Sec. 2.1) one can dismiss the fast rotating terms, and is left with

$$H'(t) = \frac{\hbar\Delta}{2} \hat{\sigma}_z + \frac{\hbar\gamma}{2} (I(t) \hat{\sigma}_x + Q(t) \hat{\sigma}_y), \quad (4.12)$$

with an additional detuning Δ which was not considered in the previous calculations, but may be added easily.

For convenience one can also rewrite this in terms of the Rabi-frequency Ω , with $\hbar = 1$, and $I(t) = \gamma I(t)/\Omega, Q(t) = \gamma Q(t)/\Omega$ (meaning that the field amplitudes of the pulses are given in Rabi-frequencies), to

$$H_{\text{RWA}} = \frac{\delta}{2} \hat{\sigma}_z + I(t) \frac{1}{2} \hat{\sigma}_x + Q(t) \frac{1}{2} \hat{\sigma}_y \quad (4.13)$$

with an effective detuning $\delta = \Delta/\Omega$ [Nb13a]. The Schrödinger-equation for this effective Hamiltonian is then the time-dependent, adjustable part for the Optimal Control technique. The I -channel induces a rotation around the x -axis, while the Q -channel induces a rotation around the y -axis.

Two different optimization goals are relevant in the context of this thesis: The first ones are pulses transferring spins from one well-defined initial state $|\Psi_i\rangle$ to another well-defined final state $|\Psi_f\rangle$ (called “transfer”-pulses), meaning that the performance measure for these kind of pulses is the overlap of a final state produced by the generated operator with an ideal final state:

$$\mathcal{F}_\delta[I(t), Q(t)] = \left| \langle \Psi_f | \mathcal{U}_{I(t), Q(t)}(t_f) | \Psi_i \rangle_\delta \right|^2, \quad (4.14)$$

where the index δ indicates that the detuning is the parameter in this case. Other

tuning parameters like the control amplitude with which the pulses are applied, may be added as well.

The other kind of pulses, are pulses optimized to implement a certain operator (therefore “operator”-pulses, e.g. a π_x rotation), that affects every state on the Bloch-sphere by the same operation, meaning that instead of the overlap between an initial and a final state, the overlap between the optimized operator and the desired operator is maximized.

Limiting physical constraints are, on one hand dephasing times, meaning that shorter pulses are generally preferred, and available power / achievable Rabi-frequencies, thus a term limiting the area under a pulse needs to be added [Nb13a].

The actual optimization algorithm, which is then done in Floquet space not for only one, but several spins, is not presented here, but may be looked up in [Nb13a] and [Bar13]. The resulting pulses are generally smoother than any pulses provided by other optimal-control techniques, have a well-defined bandwidth, and especially no high frequency components. This feature is one of the main advantages of this approach compared to other optimal control methods.

4.1.1 Simulating the dephasing environment

Using dense ensemble samples with a lot of NVs in the confocal volume, as often in the following sections, the dephasing environment, as introduced in Sec. 3.2.3 usually limits T_2 and T_2^* to several hundreds of nanoseconds. Hence, in order to get meaningful results when simulating the effect of the pulses on an ensemble of NV centers, the dephasing environment has to be taken into account.

An open quantum system, with a decoherence timescale shorter than the timescale of the experiment (Markovian bath) can be described by the so called Lindblad master-equation

$$\dot{\rho}(t) = -\frac{i}{\hbar}[H(t), \rho(t)] + \sum_n \frac{1}{2}[2C_n\rho(t)C_n^\dagger - \rho(t)C_n^\dagger C_n - C_n^\dagger C_n\rho(t)], \quad (4.15)$$

with $C_n = \sqrt{\gamma_n}c_n$ containing a coupling strength γ_n and an operator c_n describing the type of the interaction with the bath [Bre07]. The simplest form of coupling to the bath, is to choose $c_n = \hat{\sigma}_z$ leading to an exponential decay of coherence. The decay rate γ_n may be modeled as well, by using instead of a constant rate, more advanced techniques like Ornstein-Uhlenbeck noise, which is a combination of a random walk with a drift term towards a target value μ . However by increasing the number of spins, this will eventually lead to white noise again.

Evaluating the time behavior of a transfer-pulse is then pretty straightforward (this is true only in our case, and may be very tedious for more complicated Hamiltonians), by solving this Lindblad master-equation with the Hamiltonian given in Eq. 4.13 and additional collapse operators simulating the dephasing environment. This was done with

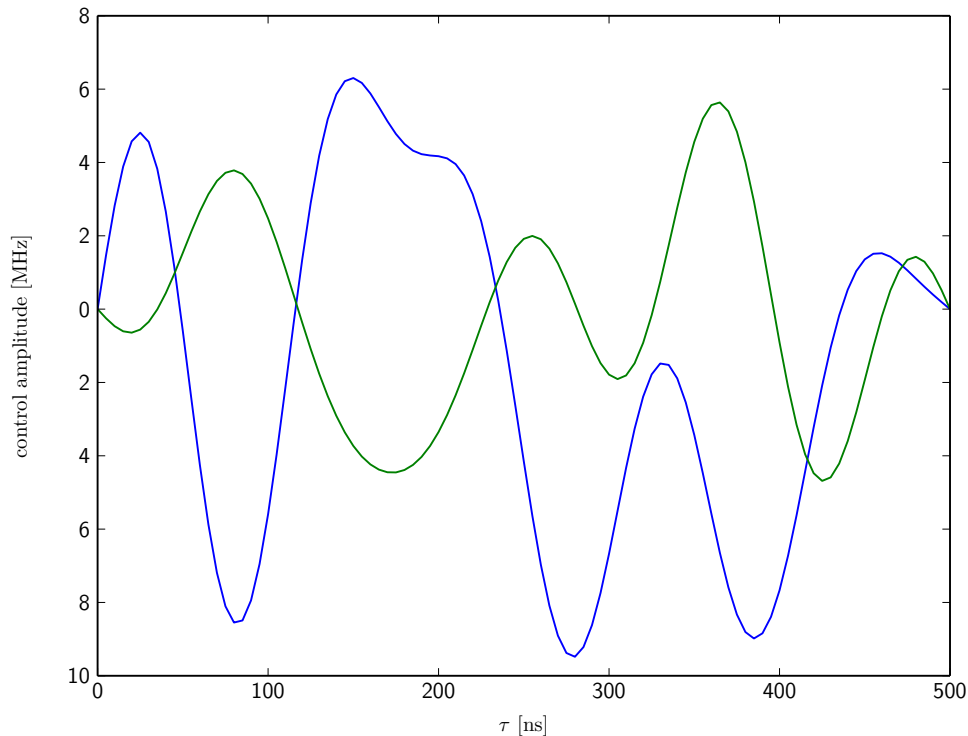


Figure 4.1: An example π -transfer-pulse (performing a $|0\rangle \rightarrow |1\rangle$ transition), using ten frequency components within a bandwidth of 25 MHz and a maximum control amplitude of 9.49 MHz. The pulse is robust for ± 4 MHz detuned spins and inhomogeneities in the control amplitude of 25%

the `qutip` package [Joh13] for the Python programming language, with an implemented master-equation solver.

Using this decoherence model, we get the trajectories in Fig. 4.2 by simulating 1000 spins with different detunings $\Delta\omega_i$ and control amplitudes and averaging over them.

Fig. 4.3 shows the temporal behavior of several detuned single spins - not averaged, but every spin with a different detuning and inaccurate control amplitude (see caption for details), simulated separately.

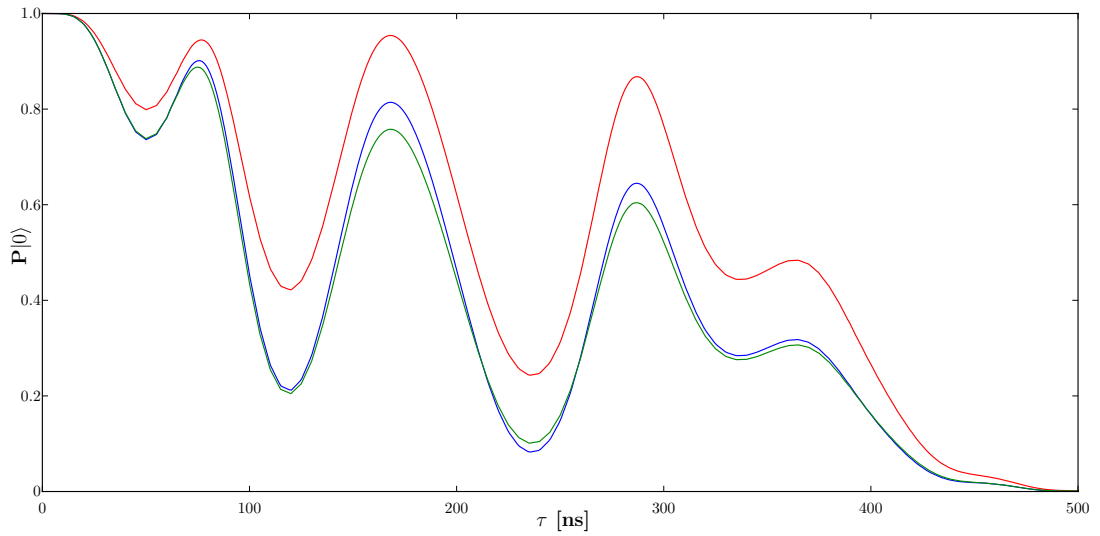


Figure 4.2: Different temporal simulations for the pulse depicted in Fig. 4.1 acting on 1000 spins with detunings of up to 10 MHz. The red curve is an averaged trajectory with no additional dephasing. The blue curve is an averaged trajectory with constant (uncorrelated) exponential dephasing and finally the green curve is an averaged trajectory with Ohrnstein-Uhlenbeck noise (finite correlation time). The trajectories are all normalized to $[0,1]$, since the trajectory does not reach zero in general with simulated dephasing. This normalization is necessary when comparing the model to experimental data, because the absolute values of the fluorescence for ensembles of NV centers are not well-defined.

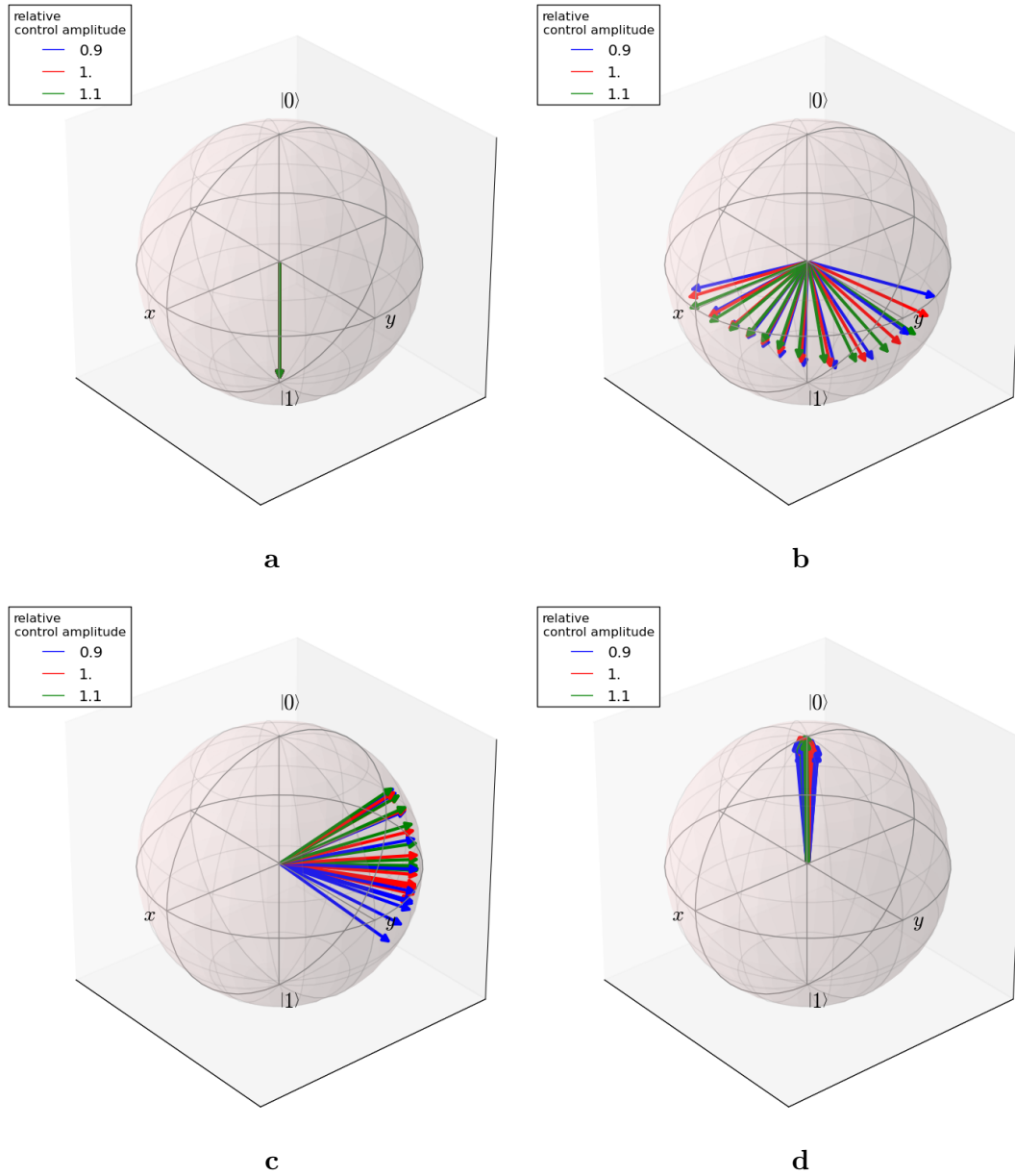


Figure 4.3: These figures show the temporal evolution of several spins with different detunings (ranging from -8 MHz to 8 MHz given by the segmentation of the arrows), and three different control amplitudes from 90% to 110% (three different colors) on the Bloch-sphere. Note however, that each of the spins was simulated separately without additional dephasing

4.2 IQ-Mixer calibration

The first step towards working with quadrature-modulated pulses (see for example Sec. 4.3) is to ensure that the playback of the pulses is correct. Assuming perfect signals from the MW-sources and the arbitrary-waveform generator (which is a valid assumption, and monitored using an oscilloscope), the device that is left to calibrate is the IQ-modulator. This IQ-modulator (Marki Microwave LMP-1545) works in a frequency-range from 1.5 GHz to 4.5 GHz covering our transition frequency, and requires a constant 13 dBm signal at the LO-port. An ideal IQ modulator modulates the two input signals $I(t)$ and $Q(t)$ onto the carrier, yielding an output signal $RF(t)$:

$$RF(t) = I(t) \cos(\omega_{LO}t) - Q(t) \sin(\omega_{LO}t), \quad (4.16)$$

so that the the I- and the Q-channel always have a relative phase-shift of 90° .

Calibrating is done by applying sinusoidal signals to the two input-channels, where each of them can be written as

$$\begin{aligned} I(t) &= (\alpha + \gamma) \cos(\omega_{IF}t) + (\beta - \delta) \sin(\omega_{IF}t) \\ Q(t) &= -(\beta + \delta) \cos(\omega_{IF}t) + (\alpha - \gamma) \sin(\omega_{IF}t). \end{aligned} \quad (4.17)$$

This representation is especially useful, when working with Fourier-components (as often in our case), and ensures that the two input signals are 90° -phase shifted as well, with ω_{IF} ranging from a few MHz to several tens of MHz. Inserting Eq. 4.17 into Eq. 4.16, and using trigonometric identities, yields:

$$RF(t) = \alpha \cos(\omega_+t) + \beta \cos(\omega_+t) + \gamma \cos(\omega_-t) + \delta \sin(\omega_-t), \quad (4.18)$$

with $\omega_+ = \omega_{LO} + \omega_{IF}$ and $\omega_- = \omega_{LO} - \omega_{IF}$.

With simple algebraic transformations one can also simplify Eq. 4.17 further to

$$\begin{aligned} I(t) &= \xi_I \cos(\omega_{IF}t - \varphi_I) \\ Q(t) &= \xi_Q \cos(\omega_{IF}t - \varphi_Q), \end{aligned} \quad (4.19)$$

with

$$\begin{aligned} \xi_I &= \sqrt{(\alpha + \gamma)^2 + (\beta - \delta)^2} \\ \xi_Q &= \sqrt{(\alpha - \gamma)^2 + (\beta + \delta)^2} \\ \varphi_I &= \arctan\left(\frac{\beta - \delta}{\alpha + \gamma}\right) \\ \varphi_Q &= \arctan\left(\frac{\alpha - \gamma}{-\beta - \delta}\right). \end{aligned} \quad (4.20)$$

The first thing needed to be calibrated, is the so called LO-leakage or LO-isolation.

This occurs because the use of hybrid junctions leads to a leakage from the LO-port to the output port, and is assumed to be frequency (ω_{IF} , i.e. the frequency at the input ports) independent, adding a constant voltage to the RF signal, which may be modeled with an additional contribution to Eq. 4.18:

$$RF(t) = I'(t) \cos(\omega_{LO}t) - Q'(t) \sin(\omega_{LO}t) + A_{LO} \cos(\omega_{LO} - \varphi_{LO}) \quad (4.21)$$

A_{LO} and φ_{LO} are the parameters that describe this LO-leakage, that is modeled to be time independent. To get rid of this unwanted signal, we simply turn off the I- and the Q-channel ($I(t) \equiv Q(t) \equiv 0$), and look at the signal still leaking to the RF-port. By adding small values of DC-voltage to the I- and Q-channel it is possible to suppress this signal down to -60 dBm:

$$\begin{aligned} I'(t) &= -A_{LO} \cos(\varphi_{LO}) = -2.2 \text{ mV} \\ Q'(t) &= A_{LO} \sin(\varphi_{LO}) = 1.13 \text{ mV}, \end{aligned} \quad (4.22)$$

resulting in $RF(t) \equiv 0$. Although this leakage is modeled to be depended of ω_{LO} , in our case it is not necessary to do this calibration more than once for one transition frequency (e.g. 2.87 GHz), because the difference in ω_{LO} hardly ever exceeds a few tens of MHz in our experiments.

To illustrate that this LO-leakage is independent of other parameters such as LO input power and the frequency of the two input ports, we use the mixer not as an up-but as a down-mixer, applying a sinusoidal signal to the RF-port of the mixer. For a perfect mixer the output at the I- and Q-channel (according to Eq. 4.16) should be two sinusoidal curves with equal amplitude and a relative phase shift of exactly 90° centered at 0 V.

The LO-leakage however, in combination with the quadrature angle error and the amplitude deviation error leads to a different signal at the I- and Q-channel. The quadrature angle error describes an error which leads to a relative phase shift of the I- and the Q-channel different from 90° , while the amplitude deviation error describes the difference in gain for each of the two input channels. This may occur due to slightly different behavior of the diodes for each channel and/or slightly different lengths of the cables within the mixer. Plotting the time behavior of $I(t)$ versus $Q(t)$ a perfect circle centered around the (0,0) coordinate would be obtained.

Instead of a circle however, the aforementioned errors lead to an ellipse centered around the DC-offsets (i.e. LO-leakage), where the ratio a/b of the main axes of the ellipse illustrate the amplitude deviation and the shift of the main axis of the ellipse with respect to the x - and y -axes illustrate the quadrature angle error. The resulting ellipses may be seen in Fig. 4.4.

Using the mixer as an down-mixer gives a first overview of the performance of the mixer, shows that there is hardly any amplitude deviation error that needs to be corrected for, and that the LO-leakage is not dependent of the input power or the frequency

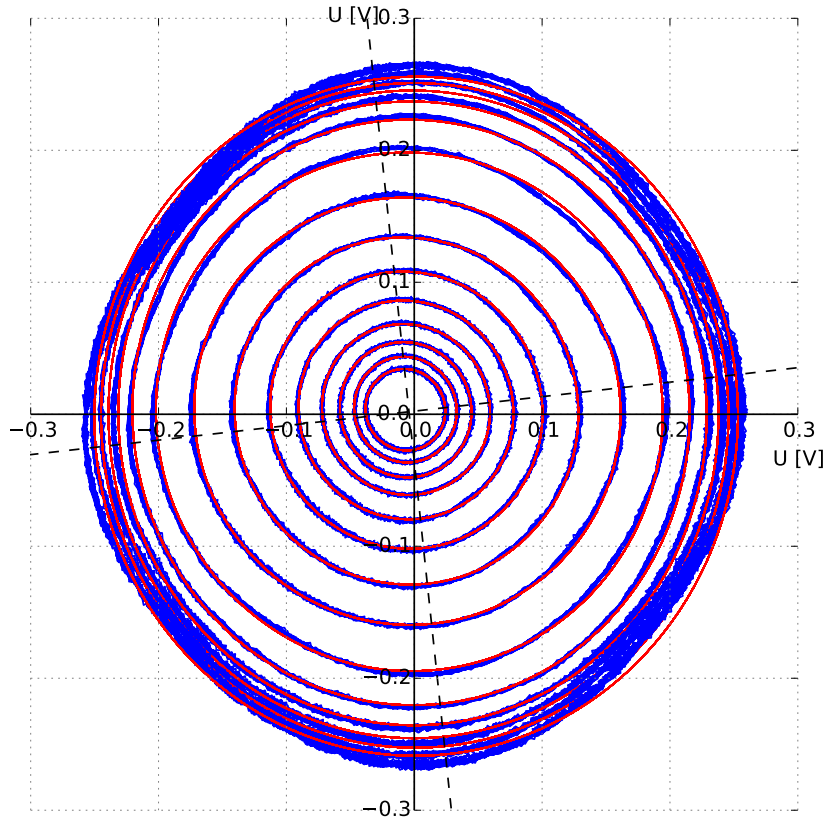


Figure 4.4: One of the resulting ellipse for the mixer calibration as described in the main text. The center of the ellipse gives directly the LO-leakage error. The dashed lines indicates the main axis of the ellipse, illustrating the quadrature-angle error, while the ratio a/b of the main axis give the amplitude deviation error. The different ellipses were recorded using different LO-powers, from -10 dBm to 20 dBm at a frequency of 2.87 GHz, showing the independence of the errors on the LO-power

at the two input ports. However, we did not use our mixer as an down- but as an up-converter, thus further calculation steps, which are necessary in order to get the exact values for the respective errors are not carried out here, but may be looked up in Ref. [Gao08].

Our approach to this problem was a little bit different by first implementing the errors into the model of the perfect mixer (the method described here was developed

by Dr. Johannes Majer and can be looked up in Ref. [Bla13]), via

$$RF(t) = I(t) \cos(\omega_{LO}t) + (1 + \varepsilon)Q(t) \sin(\omega_{LO}t - \varphi_{err}) \quad (4.23)$$

or rather

$$RF(t) = \alpha' \cos(\omega_+t) + \beta' \cos(\omega_+t) + \gamma' \cos(\omega_-t) + \delta' \sin(\omega_-t). \quad (4.24)$$

Next a linear relation between the I - and Q -channel signals and the resulting signals in the lower and upper sideband was assumed, leading to following expression when using Eq. 4.18 and Eq. 4.24

$$\begin{pmatrix} \alpha' \\ \beta' \\ \gamma' \\ \delta' \end{pmatrix} = \frac{1}{2} \begin{pmatrix} 1 + (1 + \varepsilon) \cos(\varphi_{err}) & -(1 + \varepsilon) \sin(\varphi_{err}) & 1 - (1 + \varepsilon) \cos(\varphi_{err}) & -(1 + \varepsilon) \sin(\varphi_{err}) \\ (1 + \varepsilon) \sin(\varphi_{err}) & 1 + (1 + \varepsilon) \cos(\varphi_{err}) & -(1 + \varepsilon) \sin(\varphi_{err}) & -(1 - (1 + \varepsilon) \cos(\varphi_{err})) \\ 1 - (1 + \varepsilon) \cos(\varphi_{err}) & -(1 + \varepsilon) \sin(\varphi_{err}) & 1 + (1 + \varepsilon) \cos(\varphi_{err}) & -(1 + \varepsilon) \sin(\varphi_{err}) \\ -(1 + \varepsilon) \sin(\varphi_{err}) & -(1 - (1 + \varepsilon) \cos(\varphi_{err})) & (1 + \varepsilon) \sin(\varphi_{err}) & 1 + (1 + \varepsilon) \cos(\varphi_{err}) \end{pmatrix} \begin{pmatrix} \alpha \\ \beta \\ \gamma \\ \delta \end{pmatrix}, \quad (4.25)$$

where the primed variables denote the resulting signal, whereas the unprimed variables stand for the desired or input signals. This matrix may then be simplified by taking the lowest order of the matrix, because the errors are supposed to be small ($\varepsilon \ll 1$, $\varphi \ll 1$). This results in a matrix which describes the linear relationship between the applied input signal and the resulting output signal

$$\begin{pmatrix} \alpha' \\ \beta' \\ \gamma' \\ \delta' \end{pmatrix} = \frac{1}{2} \begin{pmatrix} 2 & -\varphi_{err} & -\varepsilon & -\varphi_{err} \\ \varphi_{err} & 2 & -\varphi_{err} & \varepsilon \\ -\varepsilon & -\varphi_{err} & 2 & -\varphi_{err} \\ -\varphi_{err} & \varepsilon & \varphi_{err} & 2 \end{pmatrix} \begin{pmatrix} \alpha \\ \beta \\ \gamma \\ \delta \end{pmatrix}. \quad (4.26)$$

Determining the mixer-errors φ_{err} and ε , was then done by applying the signal

$$\mathbf{S} = \begin{pmatrix} \alpha_0 \\ 0 \\ 0 \\ 0 \end{pmatrix}, \quad (4.27)$$

resulting in an answer of the device given by

$$\mathbf{S}' = \frac{1}{2} \begin{pmatrix} 2\alpha_0 \\ \varphi_{err}\alpha_0 \\ -\varepsilon\alpha_0 \\ -\varphi\alpha_0 \end{pmatrix}. \quad (4.28)$$

Using Eq. 4.24 it is trivial to see, that the power in the upper sideband is given by

$P_+ = \alpha'^2 + \beta'^2$ and the power in the lower sideband by $P_- = \gamma'^2 + \delta'^2$. Hence

$$P_- = \frac{1}{4} (\varepsilon^2 + \varphi_{err}^2) \alpha_0^2 \quad (4.29)$$

which is non-zero in general. By applying the signal

$$\mathbf{S} = \begin{pmatrix} \alpha_0 \\ 0 \\ \gamma_c \\ \delta_c \end{pmatrix}, \quad (4.30)$$

with small γ_c and δ_c , and trying to minimize the signal in the lower sideband (to get $P_- \equiv 0$), dismissing all errors of second order, the final results can be taken from Eq. 4.24 and $P_- = \gamma'^2 + \delta'^2 = 0$:

$$\delta_c (-2\alpha_0\varphi_{err} + \delta_c) + \gamma_c (-2\alpha_0\varepsilon + \gamma_c) = 0 \quad (4.31)$$

This means that the resulting errors are given by

$$\begin{aligned} \varphi_{err} &= \frac{\delta_c}{2\alpha_0} \\ \varepsilon &= \frac{\gamma_c}{2\alpha_0} \end{aligned} \quad (4.32)$$

This procedure was carried out for several different frequencies (ω_{IF}) giving the frequency dependent errors. For the mixer we used in our experiment, we did not see an amplitude deviation relevant to our results (the lack of this error can also be seen in Fig. 4.4), whereas the quadrature angle error was big enough to alter our results. The frequency dependent error is given by $2.3^\circ + 0.03^\circ * \omega_{if}[\text{MHz}]$ and increases for higher frequencies.

If the errors are known one can invert the matrix in Eq. 4.26 to correct for them and get the wished output signal α, β, γ and δ by applying corrected input signals:

$$\begin{pmatrix} \alpha \\ \beta \\ \gamma \\ \delta \end{pmatrix} = \frac{1}{2} \begin{pmatrix} 2 & \varphi_{err} & \varepsilon & \varphi_{err} \\ -\varphi_{err} & 2 & \varphi_{err} & -\varepsilon \\ \varepsilon & \varphi_{err} & 2 & \varphi_{err} \\ \varphi_{err} & -\varepsilon & -\varphi_{err} & 2 \end{pmatrix} \begin{pmatrix} \alpha' \\ \beta' \\ \gamma' \\ \delta' \end{pmatrix}. \quad (4.33)$$

Using this matrix we can easily correct quadrature modulated pulses, by correcting for each Fourier component within a pulse and getting back the correct frequency and amplitude in order to obtain correctly shaped pulses after the MW-amplifier. The effect of such a correction is depicted in Fig. 4.5.

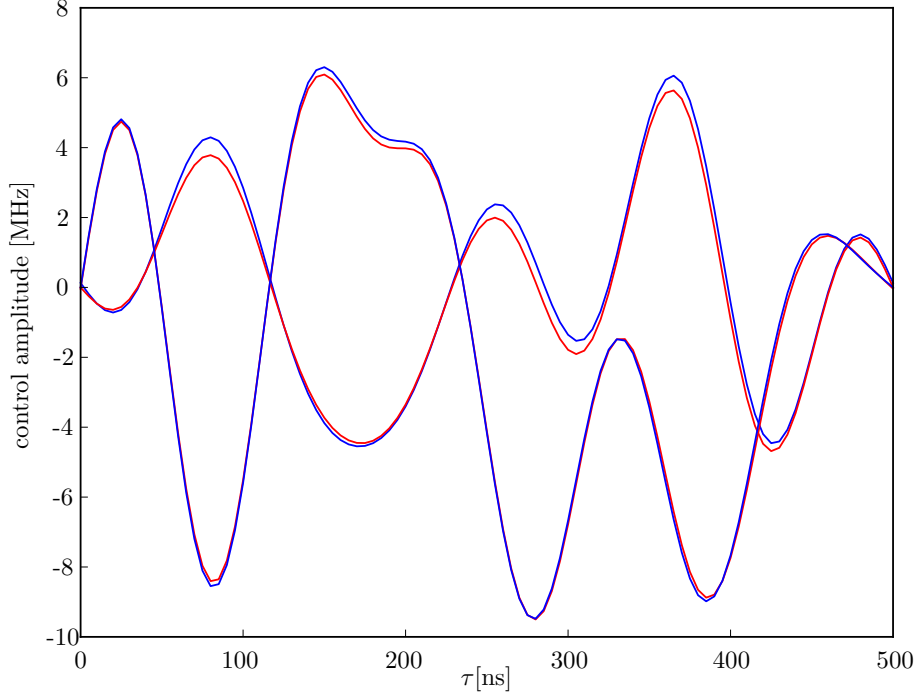


Figure 4.5: Example of a pulse-correction, with DC-offset, quadrature angle error and amplitude deviation corrected, using the method described above. The blue lines are the uncorrected pulses for each channel, compared to the corrected red ones, after multiplying with the matrix in Eq. 4.33. The amplitudes of the pulses are given in units of Rabi-frequencies.

4.3 Single NV measurements

After understanding the theory and correcting for errors in the measurement setup, the next logical step towards serious experimenting with the SOC-pulses is to look at experimental data and compare it to theoretical predictions, i.e. validate them. Since complete dynamics of inhomogeneously broadened spins in a nitrogen rich environment is difficult to simulate exactly, and simulation time is also a limiting factor, this was not done by applying the pulses onto an ensemble of spins, but rather by looking at the effects on a single NV-center.

Since working with a single NV-center always means coupling to surrounding nuclei, a method for avoiding the hyperfine-structure, as introduced in Sec. 2.4 was developed, and is described in Sec. 4.3.2.

Simulations for transfer-pulses can be carried out, and are comparatively easy to do (even more so for a single spin), since they have a well defined initial and final state (see

Sec. 4.3.3 and Sec. 4.3.4). For operator pulses, simulation is a lot harder, though. The lack of a predefined initial and final state makes it necessary to use a different approach, and therefore quantum process tomography was done as described in Sec. 4.3.5.

In order to obtain high fluorescence count rates, it is desirable to use NVs close to the surface. For the experiments described in the following, we had to use a type-2a CVD sample named “B1” which unfortunately has very few natural abundant NVs. The search for sufficient good single NVs was the most tedious part of experimenting with single NVs, and the main limiting factor when doing experiments with them.

4.3.1 Measurement sequence

The general measurement scheme for applying SOC-pulses to an NV-center is generally the same as described in Sec. 3.2.5. The spin is initialized in the $m_s = 0$ state by shining in the excitation laser. Afterwards the pulse is applied using the microwave-chain and read out using the fluorescence difference between the ground and excited state.

4.3.2 “Spin-selection” scheme

Working with a single NV-center always results in working with 3 (without surrounding ^{13}C -atoms) or more hyperfine transitions (see Sec. 2.4). To validate the pulses this is undesired, since multi-qubit dynamics is not as intuitive and easy to simulate as simple two-level systems. Thus it was necessary to develop a measurement scheme to get rid of the unwanted transitions.

For this scheme a relatively strong magnetic field along the NV-axis is required, to get a difference in resonance-frequency for the $m_s = -1$ and $m_s = +1$ state of several tens of MHz, using the m_s -dependent Zeeman-shift. This means, that a relatively strong magnetic field of $\simeq 20$ G along the NV-axis was used.

$$H_{Zeeman} = \pm \frac{2.8 \text{ MHz}}{\text{G}} \quad (4.34)$$

For the scheme itself, prior to applying the SOC-pulses, two additional pulses are necessary. The first pulse, a “strong” π -pulse with frequency ω_1 (see Fig. 4.6), transfers all spins, including the one we want to do our experiments with, to the $m_s = -1$ state (labeled ① in Fig. 4.7). Then a “weak”, selective π -pulse is used to transfer only one of this spins back to the $m_s = 0$ state leaving the other spins in the $m_s = -1$ state (②).

“Strong” and “weak” pulse refers to the power broadening of the respective pulses. By using pulses with a very high Rabi-frequency (“strong” pulses), the power-broadening of the pulse exceeds the inhomogeneous linewidth and the splitting due to hyperfine coupling by a multiple and rotates each spin similarly. A “weak” pulse however is a

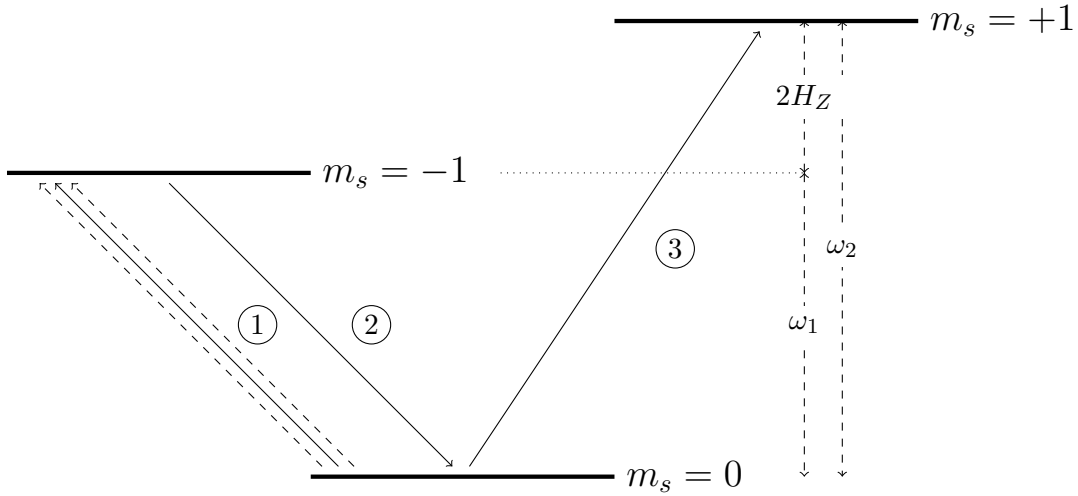


Figure 4.6: "Spin-selection"-scheme. Details are given in the main text

pulse with a low Rabi-frequency with little or no power-broadening, and thus rotating only one spin on the Bloch-sphere.

This gives us then the possibility to do our experiments (such as evaluating SOC-pulses), with only one spin with a transition frequency ω_2 (③).

Since spin-flips are rare (they occur on a timescale T_1 (i.e. the lifetime of the state) which may be around several milliseconds), this procedure is very well suited even for longer measurements.

The drawback of this technique is a worse signal to noise ratio, because we are dismissing two thirds of the signal (or even more depending on the number of transitions).

To validate that there is only one spin left, a simple FID-measurement as in Sec. 3.2.5.2 can be done, showing the number of different frequencies participating in the measurement by the number of sines necessary to fit the data. This measurement was done, showing the expected results as described in the caption of Fig. 4.7.

All subsequent single-NV measurements were done with this "spin-selection" scheme and thus involve only exactly one two-level system.

4.3.3 Experimental data versus simulation

After making sure that we are only working with one spin, verifying the effect of the pulse during the playback on a single spin is the next step. This was done by simply interrupting the playback of the pulse at different times, and reading out the state via time-resolved fluorescence counting.

Fig. 4.8 shows the simulated curve (with exponential dephasing) compared to experimental data. The good agreement between these two trajectories gives rise to the assumption that at least transfer-pulses perform as expected and may be used in other

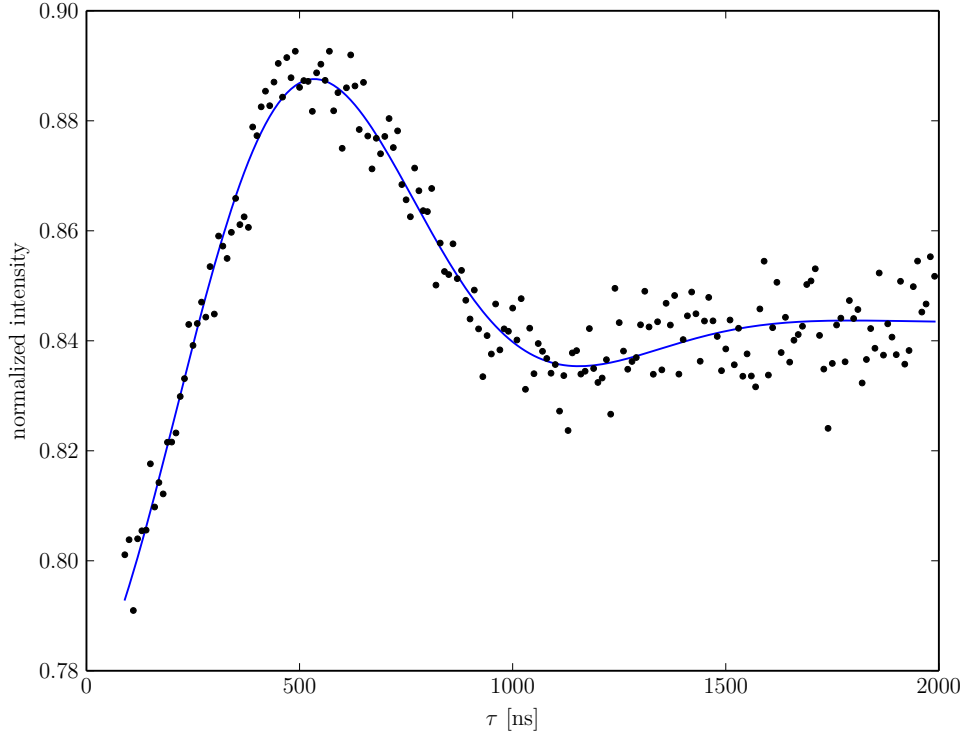


Figure 4.7: FID-measurement after the polarization with the “spin-selection” scheme. This was the exact same measurement with the same NV-center as in Fig. 3.5b, but fitted with only one sine. The measurement was done for a 1 MHz detuned driving field, to show the sinusoidal behavior and not only the exponential decay that would be present for a resonant measurement

measurements. As stated before, an evaluation of a transfer pulse with an inhomogeneously broadened ensemble of spins is harder to do, because of the non-trivial behavior of the dephasing environment, which does not simply consist of white noise as stated in Sec. 4.1.1. The effect of the same pulse on an ensemble of spins is given in Sec. 4.4.

4.3.4 Fidelity plot

Obviously the measurement in the previous section does not imply that the pulse is working for the theoretically predicted detuning and/or control amplitude range, but only at 0 MHz detuning and 100% control amplitude. To verify that the pulse is robust for the theoretically predicted parameter region, we scanned these two parameters and recorded the resulting fluorescence contrast after the pulse, i.e. the overlap of the initial and final state.

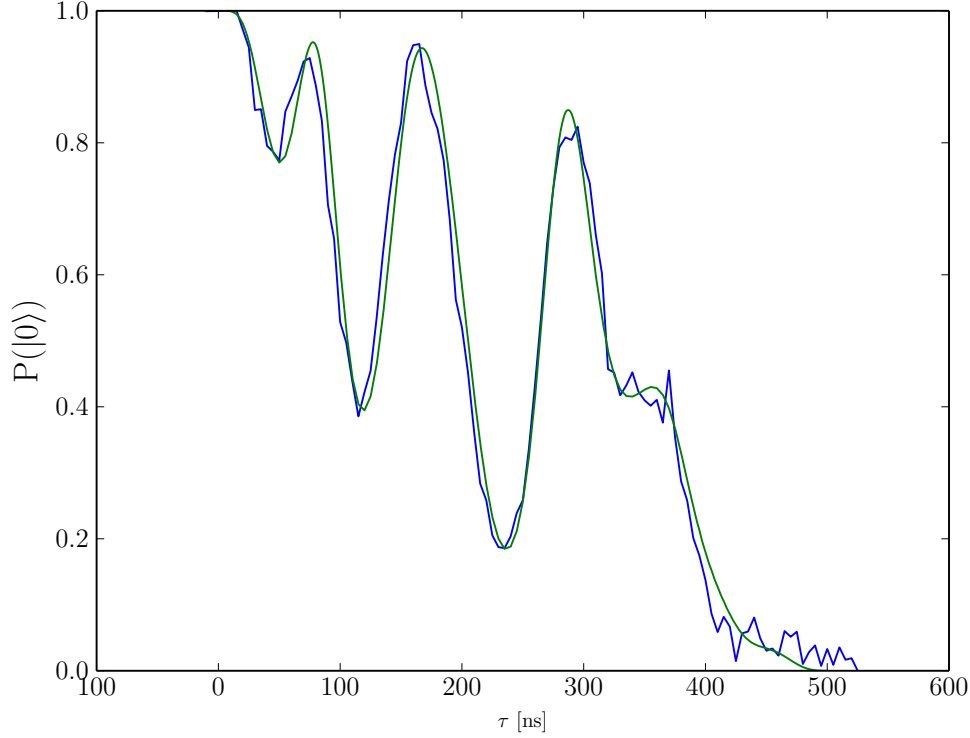
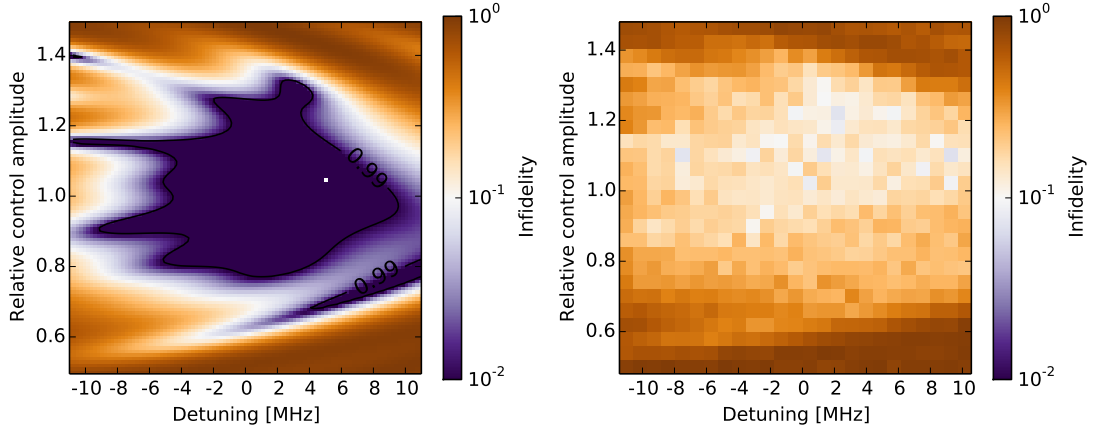


Figure 4.8: Experimental data compared to theoretical simulations. The green line indicates the theoretical simulation with additional exponential dephasing with a time-constant of $3 \mu\text{s}$, and the experimental data as solid blue line. Note that this measurement was done with only one spin

The result of this measurement is shown in Fig. 4.9. The achievable experimental resolution for contrast is on the one hand always limited by shot noise, and on the other hand by (small) imperfections in the experimental setup, such as laser-drifts, drifting of the sample etc.. The signal to noise-ratio of shot-noise limited signals increases with \sqrt{N} (the number of collected photons), and can be improved by longer measurement times, but since the number of pixels in the experimental fidelity map plays also a significant role, more than $2 \cdot 10^7$ sweeps are impractical, in order to restrict measurement times to a few days. Collecting 2-3 photons per shot, results in a total number of photons of $\simeq 3000$, and hence a shot noise of $\simeq 55$, limiting the change in contrast we can resolve to almost 3%. Thus the experimental fidelity-map may not be used to show exact agreement between theory and experiment, but can be used to show that certain features in the theoretical plot (such as the low fidelity, below 60% and above 140% of the control amplitude), can also be seen in the theoretical one.



a Theoretical fidelity plot for the same pulse as in the previous sections, showing the predicted fidelity values ranging from 50% to 150% control amplitude, and -11 MHz to 11 MHz detuning. Note that fidelities higher than 99% has been truncated, to increase readability of the plot. Simulations by B. Bartels.

b Experimental data plot, for the same parameter region as in the theoretical plot. The high and low values are normalized to the initial fluorescence after initialization, and the minimum to the minimum fluorescence (i.e. π -pulse) of a fast Rabi-oscillation.

Figure 4.9: Comparison of theoretical and experimental fidelity map. The color-scale shows the infidelity (i.e. performance) of the pulse for different detunings and control amplitudes. The scale ranges from 1 (100% infidelity) to 10^{-2} (values lower than that have been truncated). Note, that the high number of pixels in the experimental plot, leads to a very long measurement time (3-5 days depending on the number of sweeps and pixels), and hence does not allow us to further improve the shot-noise limited SNR. Nevertheless the agreement between experiment and simulation is fair, and may be even improved by longer measurements.

4.3.5 State/process tomography

After validating transfer-pulses with only one spin, the next step is to validate operator-pulses. This cannot be done by solving the Lindblad master-equation as in Sec. 4.3.3, because for operator-pulses $|\Psi_i\rangle$ and $|\Psi_f\rangle$ are not defined. This straightforward way would therefore require an infinite number of simulations and measurements.

A different (and much more suitable) approach to identify an unknown quantum dynamical process is the so called quantum process tomography (QPT), developed by G.G. Stokes in the year 1851 [Sto51] and described in Ref. [Nie00] with the experimental implementation using a NV-center in Ref. [How06].

To carry out QPT with a single qubit, a complete basis of input states has to be prepared, which we denote as $\rho_1 \dots \rho_{d^2}$, with d being the dimension of the Hilbert space (since we are working with a single NV-center $d = 2$). A convenient choice are the

states $\rho_j = |\Psi_j\rangle\langle\Psi_j|$, with $|\Psi_j\rangle = \{|0\rangle, |1\rangle, |x\rangle = \frac{1}{\sqrt{2}}(|0\rangle + |1\rangle), |y\rangle = \frac{1}{\sqrt{2}}(|0\rangle + i|1\rangle)\}$, which may be initialized using appropriate $\pi/2$ and π pulses. Preparing the state $|0\rangle$ doesn't require any additional MW-pulses, and is prepared with the excitation laser in the usual way. The state $|1\rangle$ is prepared by applying a π -pulse after the initialization in the $m_s = 0$ state, transferring the spins to the $m_s = 1$ state, whereas the states $|x\rangle$ and $|y\rangle$ are prepared by using appropriate $\pi/2$ -pulses (a rotation around the x -axis is induced by a pulse on the I -channel, while a rotation around the y -axis is induced by a pulse on the Q -channel).

After preparing the input states, the unknown process \mathcal{E} (in our case the operator-pulse) is applied to these input states, and the the resulting output states are read out, using quantum state tomography (QST).

Quantum state tomography is a way to determine an unknown quantum state. If we are given just a single copy of a quantum state, it is fundamentally impossible to reconstruct the state ρ , because there is no measurement capable of distinguishing between non-orthogonal quantum states like $|0\rangle$ and $|x\rangle$. However given a large number of copies of ρ (for example by repeating the experiment a couple of times) it is possible to estimate the state. Supposing we have many copies of the state ρ , the set

$$\begin{aligned} & \mathbb{1}/\sqrt{2}, X/\sqrt{2} \\ & Y/\sqrt{2}, Z/\sqrt{2} \end{aligned} \tag{4.35}$$

forms an orthonormal basis of the Hilbert-space. Thus ρ may be expanded in terms of this basis:

$$\rho = \frac{\text{tr}(\rho)\mathbb{1} + \text{tr}(X\rho)X + \text{tr}(Y\rho)Y + \text{tr}(Z\rho)Z}{2}, \tag{4.36}$$

with the Pauli-X gate, the Pauli-Y gate and Pauli-Z gate as introduced in Sec. 2.1.2. From basic quantum physics, we know that $\text{tr}(A\rho)$ has the meaning of an expectation value of the observable A . For example by measuring the observable Z multiple times, obtaining outcomes z_1, \dots, z_n all equal to $+1$ or -1 , the mean of these values $\sum_n z_n/n$ is then an estimate of $\text{tr}(Z\rho)$. For an increasing number of measurements, the standard deviation of the estimation improves like $1/\sqrt{n}$ [Nie00] (with n the number of total outcomes). Analogously, one can get $\text{tr}(Y\rho)$ and $\text{tr}(X\rho)$, and ends up with

$$\rho = \frac{1}{2}\mathbb{1} + \frac{1}{2n} \sum_n (x_n X + y_n Y + z_n Z), \tag{4.37}$$

or

$$\rho = \frac{1}{2} \begin{pmatrix} 1 & 0 \\ 0 & 1 \end{pmatrix} + \frac{1}{2n} \sum_n \begin{pmatrix} z_n & x_n - iy_n \\ x_n + iy_n & -z_n \end{pmatrix}, \tag{4.38}$$

with $\text{tr}(\rho) = 1$ (assuming pure states, which is valid for single NV-measurements), and the definitions above. Obtaining these output states seems straightforward by just measuring the spin-components of the corresponding operators, but needs a slightly different approach in the case of the NV-center.

Since we can only measure the z -component of the spin directly, we need to rotate the measurement basis to the z -direction, in order to obtain the x - and y -component. As an example, let us consider measuring the y -component of the spin, for the input state $|y\rangle$, with an “unknown” process, inducing a rotation of the spin around the x -axis. After preparing the spin in the $|y\rangle$ state, with an appropriate $\pi/2$ -pulse, the π_x rotation is applied, rotating the spin to the $|-y\rangle$ state on the Bloch-sphere (see Sec. 2.1.1), resulting in a y -component of the spin of -1 . However the y -component is not directly measurable in the case of a NV-center, therefore we rotate the measurement basis backwards by a $-\pi_y/2$ - (or a $3\pi_y/2$ -) pulse, and measure the z -component of the final state, yielding -1 , which can then be identified as the y -component of the output state. This can be done analogously for the x -component, whereas the z -component may be measured directly. By measuring all three components and using the standard state tomography technique as in Eq. 4.37, we are able to reconstruct the four output states $\mathcal{E}(\rho_j)$.

In principle this would suffice, and the $\mathcal{E}(\rho_j)$ should be physically valid density matrices, but in practice we would like to obtain a more useful representation of \mathcal{E} from our experimental data. Our goal is to write down a simple representation (known as Kraus-representation) with a set of operation elements $\{E_i\}$, for \mathcal{E} ,

$$\mathcal{E}(\rho) = \sum_{i=1}^{d^2} E_i \rho E_i^\dagger, \quad (4.39)$$

giving us additionally the certainty of a physically valid process (completely positive etc.).

However the E_i are operators and therefore not measurable but a theoretical construct. Thus we need a different representation with a fixed set of basis-operators A_i to rewrite Eq. 4.39 to

$$\mathcal{E}(\rho) = \sum_{m,n=1}^{d^2} \chi_{mn} A_m \rho A_n^\dagger, \quad (4.40)$$

where χ_{mn} is a matrix of coefficients, completely describing the process, and positive definite and Hermitian by construction. The matrix χ_{mn} is what we are after, because it describes how much each $A_m \rho A_n^\dagger$ contributes to $\mathcal{E}(\rho_j)$. The completeness relation

$$\sum_i E_i E_i^\dagger = \mathbb{1} \quad (4.41)$$

becomes

$$\sum_{m,n=1}^{d^2} \chi_{m,n} A_m A_n^\dagger = \mathbb{1} \quad (4.42)$$

In general χ_{mn} consists of $d^4 - d^2$ entries, because a general linear map of $d \times d$ complex matrices is described by d^4 complex parameters with d^2 additional constraints given by the completeness relation.

The general procedure works as follows: Let $1 \leq \rho_j \leq d^2$ be a fixed linearly independent basis set for a $d \times d$ matrix. A very convenient choice is the set of operators $|n\rangle\langle m|$ ($n, m = 0, 1$). The output states $\rho'_j = \mathcal{E}(\rho_j)$ may then be obtained by the aforementioned QST with the defined input states, and the identity:

$$\mathcal{E}(|n\rangle\langle m|) = \mathcal{E}(|+\rangle\langle +|) + i\mathcal{E}(|-\rangle\langle -|) - \frac{1+i}{2}\mathcal{E}(|n\rangle\langle n|) - \frac{1+i}{2}\mathcal{E}(|m\rangle\langle m|), \quad (4.43)$$

resulting in states ρ'_j that can be easily identified. Furthermore, since the ρ_j do form a linear independent, complete basis per definition, each state $\mathcal{E}(\rho_j)$ can also be represented using

$$\mathcal{E}(\rho_j) = \sum_k \lambda_{jk} \rho_k. \quad (4.44)$$

Since the states $\mathcal{E}(\rho_j)$ are known from QST, λ_{jk} can thus be calculated.

Not only $\mathcal{E}(\rho_j)$ can be represented in this basis, but also

$$\sum_{m,n=1}^{d^2} \chi_{mn} A_m \rho A_n^\dagger = \sum_k \beta_{jk}^{mn} \rho_k \quad (4.45)$$

is valid, leading to

$$\sum_k \sum_{m,n=1}^{d^2} \chi_{mn} \beta_{jk}^{mn} \rho_k = \sum_k \lambda_{jk} \rho_k, \quad (4.46)$$

or due to the linear independence for each k

$$\sum_{m,n=1}^{d^2} \chi_{mn} \beta_{jk}^{mn} = \lambda_{jk}. \quad (4.47)$$

This relation is a necessary and sufficient condition for the matrix χ to give the correct quantum operation \mathcal{E} [Nie00].

The experimental realization was done with the aforementioned input states and π_x -

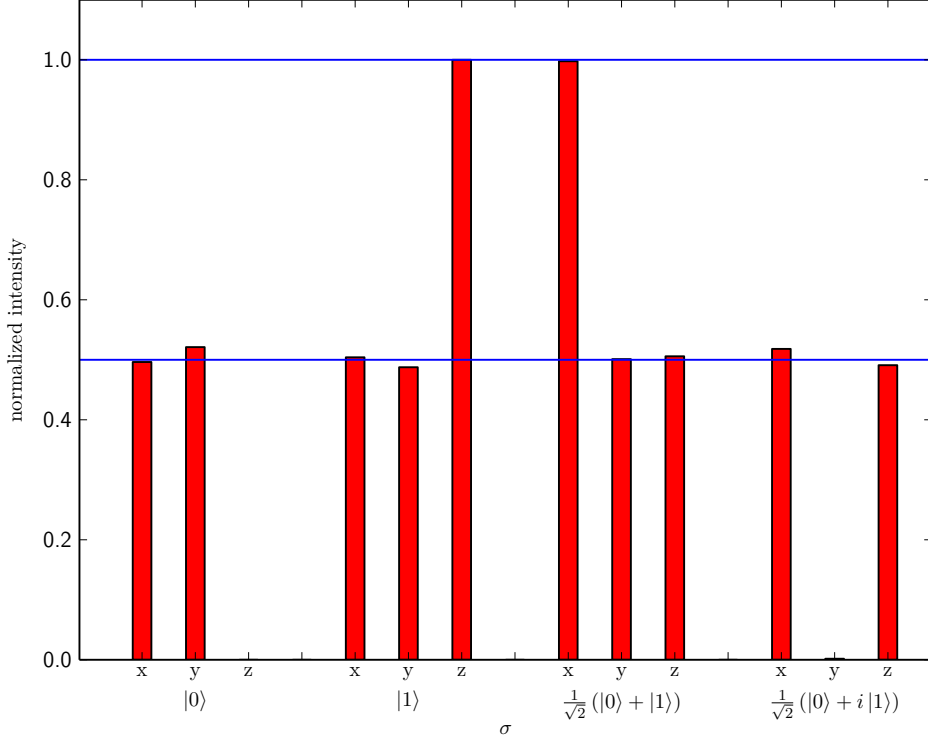


Figure 4.10: Quantum state tomography as described in the main text. On the four input states, as depicted in the picture, a π_x operation is applied. The blue lines indicate the fluorescence of the $m_s = 1$ and the superposition state of $m_s = 0$ and $m_s = \pm 1$, with the data normalized to $[0,1]$. Considering for example the input state $|0\rangle$, one gets after a π_x rotation $m_s = -1$ (fluorescence minimum), for the z -direction, and half the fluorescence for the two other directions respectively. With this knowledge and Eq. 4.37 and Eq. 4.43 one can then reconstruct the output states as necessary for the QST-technique

SOC-pulse as the process to be characterized. In the one qubit-case the most convenient choice for the basis operators A_i is given by

$$\begin{aligned}
 A_1 &= \mathbb{1} \\
 A_2 &= X \\
 A_3 &= -iY \\
 A_4 &= Z.
 \end{aligned} \tag{4.48}$$

QST was then done (see Fig. 4.10) reconstructing the output states $\rho'_j = \mathcal{E}(\rho_j)$ as

described in Eq. 4.43 with a complete basis set ρ_j , where $\rho_1 = \begin{pmatrix} 1 & 0 \\ 0 & 0 \end{pmatrix}$, $\rho_2 = \rho_1 X$, $\rho_3 = X \rho_1$ and $\rho_4 = X \rho_1 X$ (which are nothing else than the states $|n\rangle\langle m|$). For this special choice of basis, the representation for β , λ and χ simplifies to

$$\lambda = \frac{1}{2} \begin{pmatrix} \mathbb{1} & X \\ X & -\mathbb{1} \end{pmatrix}, \quad (4.49)$$

$\beta = \lambda \otimes \lambda$ and χ to [Nie00]

$$\chi = \lambda \begin{pmatrix} \rho'_1 & \rho'_2 \\ \rho'_3 & \rho'_4 \end{pmatrix} \lambda. \quad (4.50)$$

Supposing a perfect measurement with a perfect π_x -operator, using the previously described technique and specified set of basis states, χ becomes

$$\chi_{id} = \begin{pmatrix} 0 & 0 & 0 & 0 \\ 0 & 1 & 0 & 0 \\ 0 & 0 & 0 & 0 \\ 0 & 0 & 0 & 0 \end{pmatrix}, \quad (4.51)$$

and consequently

$$\mathcal{E}_{id}(\rho) = X \rho X, \quad (4.52)$$

which describes nothing else than a NOT-gate.

After looking at the response of a complete basis set to an unknown process, other interesting quantities need to be evaluated. Of particular importance is the fidelity, describing how closely the dynamics of the investigated quantum system approximates an ideal target quantum system without errors. In order to do this we need, in addition to the evaluated process matrix χ , a closely related but more abstract representation, which is provided by the Jamiolkowsk-formalism [Jam72], known as the process density matrix

$$\rho_{\mathcal{E}} = [\mathcal{J} \otimes \mathcal{E}] (|\Phi\rangle\langle\Phi|) \quad (4.53)$$

with $|\Phi\rangle = \sum_j |j\rangle |j\rangle / \sqrt{d}$ as a maximally entangled state of the (d-dimensional) system with itself, and $\{|j\rangle\}$ an orthonormal basis-set [Chu97]. This can be simplified to

$$\rho_{\mathcal{E}} = \frac{1}{2} \sum_{ij} |i\rangle\langle j| \otimes \mathcal{E}(|i\rangle\langle j|). \quad (4.54)$$

For the ideal case we obtain

$$\rho_{id} = \frac{1}{2} \begin{pmatrix} 0 & 0 & 0 & 0 \\ 0 & 1 & 1 & 0 \\ 0 & 1 & 1 & 0 \\ 0 & 0 & 0 & 0 \end{pmatrix}. \quad (4.55)$$

Given now these two density matrices, one for the ideal (ρ_{id}) and one for the experimental case ($\rho_{\mathcal{E}}$), we can define the fidelity of the experimental density matrix as the distance between the experimental density matrix and the ideal one [Chu97]

$$\mathcal{F}(\rho_{id}, \rho_{\mathcal{E}}) = \text{tr} \left(\sqrt{\sqrt{\rho_{id}} \rho_{\mathcal{E}} \sqrt{\rho_{id}}} \right)^2 \quad (4.56)$$

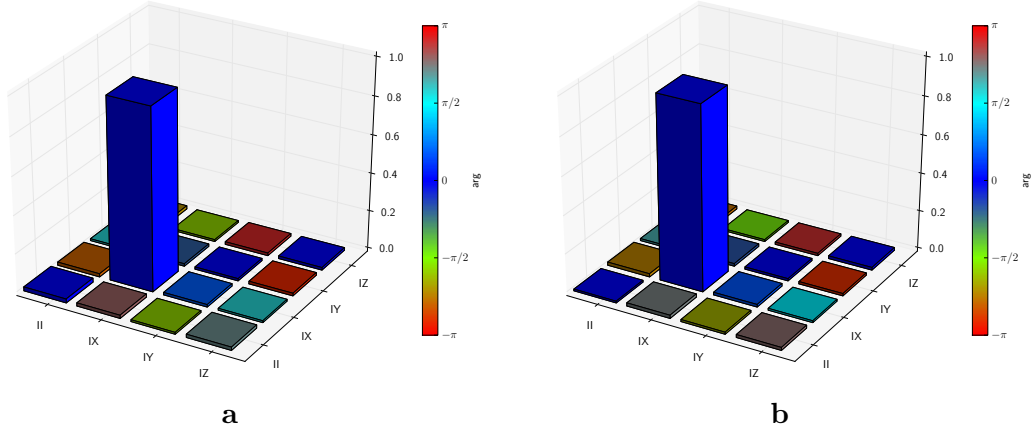


Figure 4.11: Quantum process tomography as described in the main text for a process inducing a π_x rotation. The height of the columns represents the complex amplitude of the corresponding matrix element of the process χ -matrix, whereas the color represents the complex phase. These two figures show two different measurements, Fig. 4.11a a process tomography measurement with a SOC- π_x pulse, played at 75% of the ideal control amplitude, whereas Fig. 4.11b shows the same measurement but with 100% control amplitude. Resulting fidelities are given in the main text

This experiment was done for two cases using a π_x -SOC-operator as the process to evaluate: First the pulse was played with 100% control amplitude (i.e. the center of the range of control amplitudes for which the pulse was designed to be robust), resulting in

a process matrix depicted in 4.11b, numerically given as (without the imaginary part)

$$\chi = \begin{pmatrix} 0.0093 & -0.0117 & 0.0046 & -0.0118 \\ -0.0117 & 0.9647 & 0.0118 & 0.0009 \\ -0.0046 & 0.0118 & 0.0118 & -0.0117 \\ -0.0117 & 0.0009 & -0.0017 & 0.0014 \end{pmatrix}$$

and a resulting fidelity of

$$\mathcal{F} = 0.9647.$$

For 75% of the control amplitude as depicted in 4.11a, the resulting fidelity was not much worse, but still

$$\mathcal{F} = 0.9535,$$

indicating that the SOC-pulse is robust with respect to inaccuracies in the control amplitude, since only 1% percent of overall fidelity was lost.

The results however do not give the absolute fidelity of the SOC-pulse, because not only errors from the pulse, but also errors occurring from the preparation and readout-pulses are combined in this value. Nevertheless with careful experimentation, we believe that the errors occurring from the rectangular “hard”-pulses are rather small (note that this is only true for a single qubit) and the resulting infidelity of about 4-5% mainly occurs due to the SOC-pulse.

A quantity, describing the experimental imperfections is the “unphysicality” of the process, as proposed in [How06]. This quantity can be characterized examining the eigenvalues of χ . If one or more of these eigenvalues are negative, this indicates that noise, finite sampling and/or other imperfections caused the output data to induce an unphysical process. To get rid of the “unphysical” part of the process matrix we define a physically valid process matrix $\tilde{\chi}$ which is, in a sense, as close as possible to the original process matrix χ , but with real and positive eigenvalues.

We define[How06]

$$T(t) = \begin{pmatrix} t_1 & 0 & 0 & 0 \\ t_5 + it_6 & t_2 & 0 & 0 \\ t_{11} + it_{12} & t_7 + it_8 & t_3 & 0 \\ t_{15} + it_{16} & t_{13} + it_{14} & t_9 + it_{10} & t_4 \end{pmatrix} \quad (4.57)$$

as a $d^2 \times d^2$ complex, lower triangular matrix, and

$$\tilde{\chi} = T^\dagger(t)T(t), \quad (4.58)$$

enforcing a completely positive matrix $\tilde{\chi}$. In order to get the matrix $\tilde{\chi}$, we minimize

the deviation function

$$\Delta(t) = \sum_{mn}^{d^2} |\tilde{\chi}_{mn}(t) - \chi_{mn}|^2, \quad (4.59)$$

for the 16 free parameters, under the trace preserving constraint

$$\sum_{mn}^{d^2} \tilde{\chi}_{mn}(t) A_n^\dagger A_m = \mathbb{1}. \quad (4.60)$$

Since the original process matrix χ contained eigenvalues smaller than one, this procedure was necessary and has been done, using the ‘‘Sequential Least Squares Quadratic Programming’’ (SLSQP) optimizer as implemented in the python-toolbox `scipy.optimize`.

To avoid local minima for this optimization routine and deliver acceptably good ‘‘guess’’-parameters t_i^0 for the minimization routine a preliminary ‘‘filtering’’ of the process matrix was necessary. This was done by setting all (presumably small) negative eigenvalues of χ to zero, by decomposing the matrix with,

$$\chi = UDU^\dagger \quad (4.61)$$

with D the Jordan normal form. Setting the negative eigenvalues in D to zero, and calculating

$$\chi^* = UD^*U^\dagger \quad (4.62)$$

we can extract good enough starting-parameters for the minimization problem from χ^* using Cholesky-decomposition [Gol96] (implemented in `scipy.linalg`).

With the new process matrix $\tilde{\chi}$ one can define a measure for unphysicality, by defining $X = \chi - \tilde{\chi}$, and calculating the norm thereof. Possible measures are the Frobenius norm, the matrix p-norm and/or the trace-distance D_{pro} , which are all given in table 4.1

Table 4.1: Disparity between experimental process matrix, and the closest physically valid one, for the two measurements with 100% control amplitude and 75% control amplitude

| | $\ X\ _{Fro}$ | $\ X\ _p$ | D_{pro} |
|------|---------------|-----------|-----------|
| 100% | 0.0159 | 0.01624 | 0.000127 |
| 75% | 0.01484 | 0.01618 | 0.00011 |

Note however, that these distance-measures depend on the choice of basis-operators A_i , and are therefore not an absolute quality measurement and can only be compared to QPT-measurements with a reconstructed process matrix using the same basis-operators. The small values for the unphysicality however (compared to other experiments like in [How06]) indicate that the experiment itself was well done, and that infidelities mainly

occur due to errors induced by the SOC-pulses.

4.4 NV ensemble measurements

After validating the SOC-pulses for a single NV-center, the next step is to use the pulses for an inhomogeneously broadened ensemble of spins, because as Sec. 4.3.4 suggests, that is what the pulses are designed for.

The advantage of using ensembles over single-NV centers, is the fact that per measurement shot, more photons are collected and the signal strength overall is therefore higher. Unfortunately it turns out that the more environment adds a lot of background signal to the desired signal and the SNR decreases drastically. Another drawback of ensembles of spins is the much more complicated dephasing-environment. This includes not fully understood electron dipole-dipole interactions, derating the dephasing-times (T_2^* , T_2) by more than a factor of 1000. The complicated dephasing environment makes it also almost impossible to simulate the effect of the surrounding spin-bath on the electron spins qualitatively.

Nevertheless, an inhomogeneously broadened ensemble of spins is very well suited to show the advantage of the SOC-pulses over less robust control techniques: For example, the contrast of spin flip operations can be increased drastically compared to simple rectangular pulses.

While the single-NV measurements were done with naturally occurring NV-centers, the ensemble measurements in the following sections were done using different samples: Sample BS3-3b (see Ref. [Nb13b]), a type 1b-sample, produced from a HPHT process, irradiated with neutrons and annealed in order to get high NV^- densities. This sample has been used for almost all ensemble measurements. For Sec. 4.4.2 was replaced by another one, because the decoherence times of BS3-3b are in the range of $T_2 \approx T_2^* \approx 450$ ns not long enough in order to get meaningful results.

Instead an untreated CVD sample from Delaware Diamond Knives was used. This sample combined rather high NV densities with acceptable dephasing times.

4.4.1 Power and squeeze-scans

In Sec. 4.3.4 we showed that the pulses are indeed robust for a range of different control amplitudes and detunings. However, recording a fidelity map is fruitless since a complete valid theoretical explanation of the temporal behavior is complicated to do qualitatively (although some simulations for ensembles of spins were done, see Sec. 4.1.1). Another (unwanted) side-effect of using ensembles of NV centers is the fact, that the exact characterization of the fluorescence of the $m_s = \pm 1$ state is a lot harder to do. The ideal contrast of $\approx 30\%$ can never be achieved and since the exact spin dynamics is still a partly unsolved problem, a meaningful statement on the exact fluorescence value of the excited qubit state is not possible.

Thus a complete simulation of the pulses acting on an ensemble of spins is not doable and the only meaningful comparison, is to compare the effect of the pulse for a range of different parameters.

Fig. 4.12 shows the temporal trajectories of the pulse depicted in Fig. 4.1 with the control amplitudes scaled from 72% to 134%. This “power”-scan shows once more that the pulses are robust for a range of control amplitudes not only for a single NV center but also for a lot of spins with different detunings. Although the shape of the trajectories changes, the achieved contrast (i.e. population transfer) does not increase or decrease significantly, yielding the (almost) same value for each of the different cases.

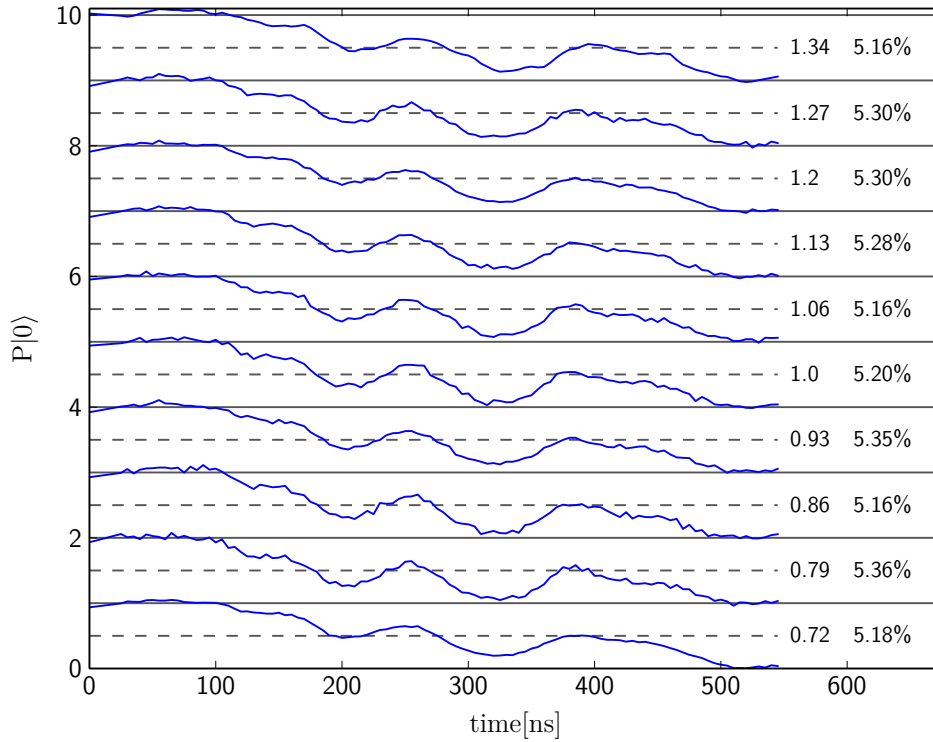


Figure 4.12: Evolution of the ensemble-averaged population in the $m_s = 0$ state during playback of a series of SOC pulses. The pulses were scaled in amplitude from 72% to 134%. The amplitude scaling factor is given to the right of the respective traces. The resulting contrast is given in terms of relative change in fluorescence in the rightmost column. There is no significant drop in contrast, showing that the pulses are robust for a change in amplitude, even for an ensemble of spins. Note that these curves are normalized to the highest and lowest values respectively, and are slightly smoothed in order not to normalize on noise

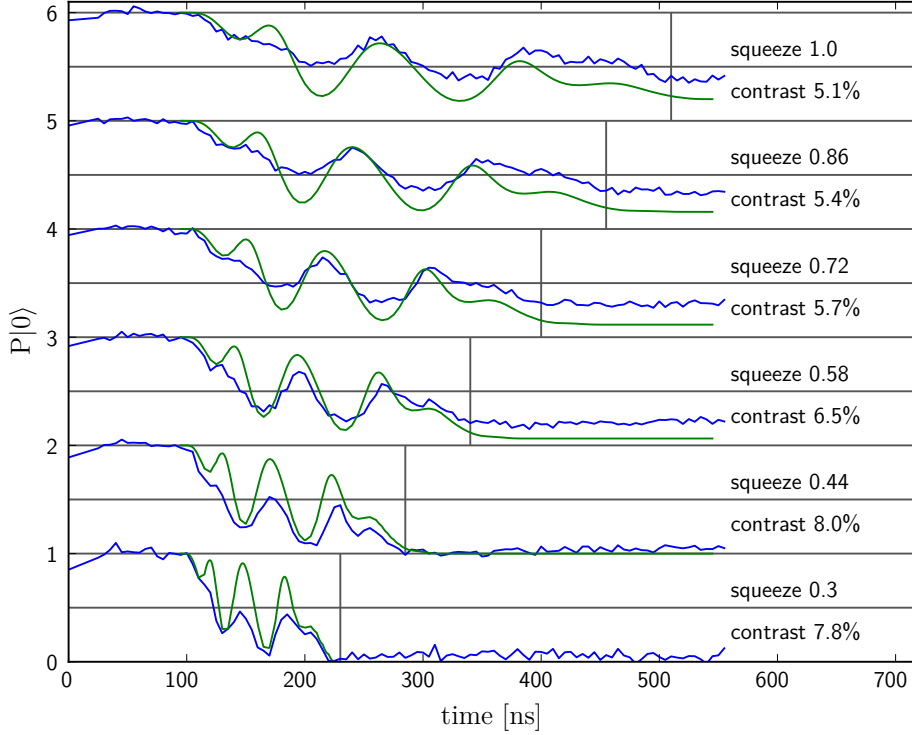


Figure 4.13: A scan performed on an ensemble of spins, for the same transfer π pulse as in the previous sections. Plotted is a range of “squeezed” trajectories, denoting that the pulses have been compressed, by the factor depicted on the right side in each row. The contrast improves significantly, because the pulses become shorter compared to the dephasing time. The green lines are simulations with simple exponential dephasing. The trajectories are normalized to the maximum contrast of all pulses, which occurs at a squeeze factor of 44%, with a contrast of 8% (compared to 30% for a single NV-center). Obviously the contrast does not increase for the last squeeze-factor, maybe due to the fact, that the achieved 8% contrast is already the maximum achievable contrast.

The pulses itself are optimized for static dephasing (i.e. inhomogeneous broadening), but not for dynamical dephasing (T_2). The shorter T_2 , the more we desire pulses that are short compared to this dynamical dephasing. However shorter pulses usually require higher Rabi-frequencies and thus higher MW powers.

We cannot influence dephasing times, since they are a material constant of each sample used, but by moving closer to the wire / gold-structures [Kow13] carrying the MW-signal, the available power at the sample changes from experiment to experiment. Calculating new pulses for each of these scenarios however is not practical since it requires computation time and resources.

Thus, in order to play back pulses as fast as possible, we can “squeeze” the pulses, while keeping the area under the pulse constant and gain a lot of contrast by reading out the state sooner. This can yield crucial improvements as shown in Fig. 4.13.

By playing back a 500 ns pulse with $\approx 30\%$ of its initial length, the contrast increases by $\approx 50\%$, which is primarily due to the fact that the pulses become shorter compared to the T_2 time. The robustness for detunings and control amplitudes increases proportionally, because the pulses are optimized in units of the control amplitude. Depending on the sample, this squeezed pulse can be twice as good as the fastest possible π pulse achievable with a rectangular pulse. For samples with very short T_2 times the improvement may be not as much, because the shortest possible rectangular pulses, may be as short as 12.5 ns (limited by the minimal pulse duration achievable with our pulse generator hardware), but for samples with T_2 times in the range of 500 ns or more there is most certainly an improvement. By comparing the SOC-pulses to equally long rectangular-pulses, the improvement is generally more than a factor of five.

Note however, that this is only true for an ensemble of spins. For single NV-centers a hard pulse is generally better, because shorter. The more inhomogeneously broadened the spin ensemble becomes, the better the SOC-pulses perform compared to hard pulses.

4.4.2 Spin-echo measurements using Smooth Optimal Control-pulses

Although it is not possible to simulate the temporal evolution of a pulse acting on an ensemble of spins quantitatively, Fig. 4.12 shows that the pulses do work for an ensemble of inhomogeneously broadened ensemble spins as intended. Therefore the next step is to look not only at the effect of a single pulse on an ensemble of spins, but perform multi-pulse sequences as introduced in Sec. 3.2.5.2 and Sec. 3.2.5.3. Instead of using rectangular pulses to perform appropriate $\pi/2$ - and π -pulses, we replace them with SOC-pulses.

The pulse sequence is exactly the same as in Fig. 3.6a, with the same pulse sequence $\pi/2 - \tau - \pi - \tau - \pi/2$. The first $\pi/2$ -pulse is a $|0\rangle \rightarrow |0\rangle + |1\rangle$ transfer pulse, because we want as much spins transferred as possible from the initial state to the equator of the Bloch-sphere. The second pulse however is necessarily not a transfer pulse: During the playback of this pulse a rotation of the spins around an axis is desired, because we want to keep the static dephasing of the spins (in fact that is the key essence of a spin-echo sequence). Therefore we used a π -operator pulse instead.

The situation for the last pulse is different. For the spin-echo sequence we wanted to achieve maximum contrast, rotating as many spins as possible to the $|0\rangle$ state with the last pulse. Thus we used a $|0\rangle \rightarrow |0\rangle + |1\rangle$ transfer pulse and reversed it to get a $|0\rangle + |1\rangle \rightarrow |0\rangle$ pulse.

This reversal of the pulse works, because for unitary transformations (which the pulses are) $U(-t)|\Psi_f\rangle = U(-t)U(t)|\Psi_i\rangle = |\Psi_i\rangle$. Hence, time reversal in this case results in a pulse which transfers spins from the final to the excited state.

It is often helpful to record the same trace with a $3\pi/2$ -pulse instead of a $\pi/2$ -pulse

in the end: In such a sequence, a phase on the equator is converted into population of the $m_s = 1$ state, and hence the contrast decreases. This gives us a mirrored trajectory, which we can use to better identify the baseline, necessary for fitting the curve. In order to obtain a $3\pi/2$, we used a reversed $|0\rangle \rightarrow |0\rangle + |1\rangle$ pulse and concatenated it with a $|0\rangle \rightarrow |1\rangle$ pulse, overall generating a $|0\rangle + |1\rangle \rightarrow |1\rangle$ pulse.

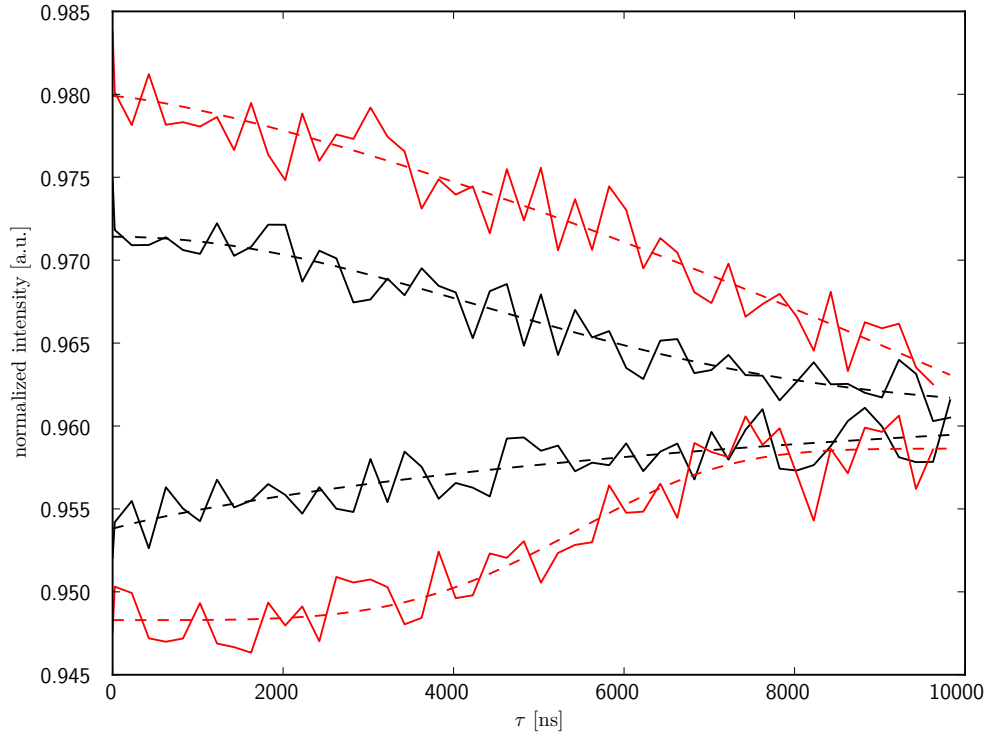


Figure 4.14: Spin-echo sequence comparing a measurement with rectangular pulses (black line) with a measurement for equally long SOC-pulses (red). The contrast roughly increases by a factor of two. Simulations has been done according to Ref. [Sta10], giving T_2 times of ~ 6000 ns. The lower trace is generated by using a $3\pi/2$ pulse at the end instead of a $\pi/2$ -pulse

The results were then compared to the same experiment with rectangular pulses, yielding an improvement in contrast as shown in Fig. 4.14 of about a factor of two. This improvement is in the range of the expected value and is comparable to the increase of contrast for only one single pulse.

5 Magnetometry using smooth optimal control

Knowing the exact Hamiltonian for the NV-center, the most straightforward way to measure magnetic fields is to look at ODMR-spectra and the positions of the resonance frequencies. While this is a valid way to measure magnetic fields that may even be improved by cleverly chopping the CW-microwave, the linewidth and thus resolution of this method is always limited by the inhomogeneous broadening $\Gamma_2^* = \frac{1}{\pi T_2^*}$. Moreover the sensitivity is also limited by the contrast of the resonance-line which means that there is always a trade-off between collecting a lot of photons for low shot noise and measurement time, as well as good SNR and power-broadening, which increases the spectral line-width [Dr11].

On the other hand interferometric measurements (as presented in this section) like the Ramsey measurement (not discussed here but can be looked up in [Nb13a]), and especially spin-echo-like magnetometry sequences, are pulsed measurements limiting the effect of power-broadening on the sensitivity, and allows us to compensate for static dephasing and thus limited by T_2 .

While ODMR-based, as well as Ramsey-based techniques are sensitive to DC-fields, the spin-echo sequence responds to an alternating external field with a frequency corresponding to a user-selectable period, the so-called free precession time. A lot of experiments using this sequence have been done, not only with single NV-centers [Maz08] but also with ensembles of spins (as in our experiment) [Pha11]. Sensing schemes with single NV-centers have an advantage over measurements with ensembles of spins because of the higher contrast and longer dephasing times, which is directly proportional to the sensitivity (see Eq. 5.8). However the higher fluorescence of ensembles of NV centers reduces shot-noise which increases the sensitivity, but unfortunately only scales with the square root of the number of photons.

5.1 Interferometric magnetic sensing using spin-echo sequences

The experimental implementation of this measurement scheme is basically the same as in Sec. 4.4.2, with the difference, that we fix the duration between two of the free pulses (τ , more on the optimal value for τ in Sec. 5.1.1), and turn on a magnetic field oscillating with a frequency corresponding to it (see Fig. 5.1). This magnetic field induces a phase shift $\Delta\phi = \int_0^{2\tau} \Delta\omega(t) dt$, with $\Delta\omega$ proportional to the applied magnetic field

$$\Delta\omega = \mu_B g B(t). \quad (5.1)$$

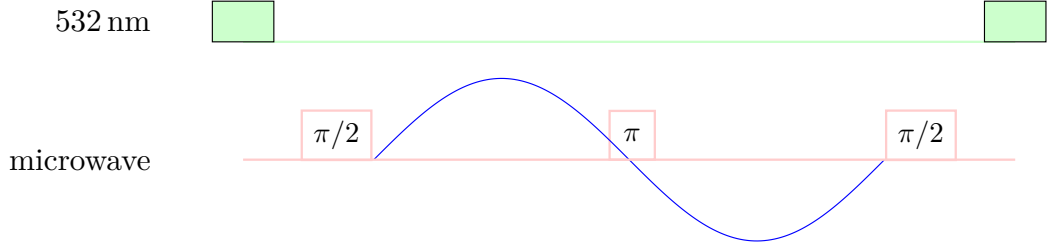


Figure 5.1: Measurement scheme for AC-field sensing using NV-centers. The scheme is basically a spin-echo sequence with the difference of the applied magnetic field (depicted as blue line). The induced phase shift $\Delta\phi$ is proportional to the area under the blue curve

The magnetic field was provided by a small homemade coil, positioned directly at the sample, providing a few Gauss of magnetic field at the position of the sample. The magnetic field was controlled with an additional AWG, capable of changing the current through the coils very quickly. Since we wanted to make the phase shift as large as possible, the area under $B(t)$ was maximized, resulting in rectangular pulses instead of the sine wave as depicted in 5.1. Thus

$$\Delta\phi = \int_0^{2\tau} \Delta\omega(t) dt = \mu_B g B_0 2\tau = 2\tau \frac{2.8 \text{ MHz}}{\text{G}} B_0 \quad (5.2)$$

By ramping up the magnetic field from zero to the maximum possible value (limited by the maximum output power of the AWG generating the coil current, the number of windings of the coil and the distance of the coil to the sample), a sinusoidal behavior of the spin-echo contrast is observed: $\Delta I \propto \cos(2\pi\Delta\phi)$ (see Fig. 5.2): If the phase shift happens to be equal to one ($\Delta\phi = 1$), the effect of the magnetic field is cancelled out and the full spin-echo contrast is recovered.

5.1.1 Minimum detectable magnetic field

The sensitivity of a sensing measurement is defined by requiring $SNR = 1$, which means that the change in signal induced by the minimum detectable field is equal to one standard deviation of the limiting noise (in our experiments always shot-noise), i.e.

$$\delta B_{min} = \frac{\sigma_{sn}}{dS}. \quad (5.3)$$

dS is the change of the signal due to the magnetic field:

$$dS = \left| \frac{\partial S}{\partial B_0} \right|. \quad (5.4)$$

The signal S is given by the sinusoidal curve in Fig. 5.2 [Dol11]:

$$S = CN_{tot} \cos(\Delta\phi), \quad (5.5)$$

where C is the spin-echo contrast (normalized to the number of photons, e.g. 0.3 for a single NV-center) and N_{tot} the total number of photons. This becomes

$$dS = |2N_{tot}C\tau\mu_Bg \sin(2\tau\mu_BgB_0)| \approx 2N_{tot}C\tau\mu_Bg, \quad (5.6)$$

because we are interested in the minimum detectable field / strongest signal, and thus $|\sin(\dots)| = 1$. The shot-noise σ_{sn} is given by $\sqrt{N_{tot}}$. The total number of photons depends on several other parameters

$$N_{tot} = N_{ps} \frac{t_{acq}}{(2\tau + t_{prep})s} T, \quad (5.7)$$

where t_{acq} is the time-span per shot for which photons are collected (usually 200 ns, see Sec. 2.3.1.2 for more details), N_{ps} the photon counts per second, s the number of measurement steps (i.e. magnetic field steps), T the total measurement time, and t_{prep} the duration for one shot for each measurement point (the free precession time 2τ excluded). The duration of the pulses as well as the time for initialization and read-out are merged into this parameter.

The overall sensitivity for the total measurement time T is therefore the quantity

$$\delta B_{min} = \frac{1}{C\mu_Bg\sqrt{N_{tot}}}. \quad (5.8)$$

Dividing by \sqrt{T} and the square root of the confocal volume $\sqrt{V_{conf}}$ (i.e. measurement volume, which is $2.3 \mu\text{m}^3$ in our setup) gives the sensitivity per square root second and square root cubic meter, which is a good absolute measure for the sensitivity [Pha11]

$$\delta B_{min} [\text{T Hz}^{-1/2} \text{cm}^{-3/2}] = \frac{1}{C\mu_Bg\sqrt{N_{tot}}\sqrt{TV_{conf}}}. \quad (5.9)$$

This equation shows the problems of measurements with ensembles of spins compared to measurements with single NV centers. We lose approximately a factor 10 or more in contrast (1-3% instead of 20%), and approximately a factor 100 for τ (3 μs instead of 300 μs), with the only advantage in the higher number of photons N . In order to get the same or better sensitivity, \sqrt{N} needs to become larger by a factor of ≈ 50000 .

In order to find the ideal value for the free-precession time τ to get the maximum sensitivity, it is necessary to minimize δB_{min} with respect to τ ,

$$\frac{\partial \delta B_{min}}{\partial \tau} = 0. \quad (5.10)$$

Unfortunately however with increasing τ , the contrast C decays. The exact shape of that decay is dependent on the sample and experimental parameters. The decay shape may be modeled by [Sta10]

$$C(\tau) = C_0 e^{-\left(\frac{\tau}{T_2}\right)^n}, \quad (5.11)$$

where n is the fit parameter and usually between 1 and 2 (depending on e.g. the exact orientation of the magnetic field). The equation to solve, thus becomes

$$\frac{2n \left(\frac{\tau}{T_2}\right)^n - 1}{2\tau^{3/2}} = 0, \quad (5.12)$$

yielding $\tau \approx 0.5T_2$.

After calculating all the necessary parameters, Eq. 5.9 leaves us with three different ways to calculate the sensitivity:

1. The most straightforward way in order to calculate the sensitivity is to use Eq. 5.9 and inserting Eq. 5.7 for N_{tot} . This method is the “theoretical” method, which allows us to compare our experimental data to the theoretical predictions.
2. Apart from calculating the total number of photons for each measurement point with equation 5.7, we can also get N_{tot} by looking at the integrated count data, collected for one measurement point during the whole measurement time. This turns out to be the choice closer to the experimental data, because it relies only on data directly available and less parameters (“semi-theoretical” method).
3. The third and probably easiest way to calculate the sensitivity, is to look at the raw data of the signal, calculating the standard deviation of it (by looking at the residuals) and the slope of the signal. These quantities can then be identified directly as σ_{sn} and dS . By multiplying with the total measurement time and the confocal volume, we get the same quantity as before.

5.1.2 Sensing using smooth optimal control

Sec. 4.4.2 already indicates that using SOC-pulses instead of rectangular pulses increases the achievable spin-echo contrast and consequently increases the sensitivity. Thus, for further improvement of the measurement scheme, especially when working with samples with a large inhomogeneous broadening, three SOC-pulses instead of three rectangular pulses are used.

The sole difference of this measurement scheme, apart from the magnetic field, compared to the spin-echo scheme described in Sec. 4.4.2, is the fact that the last $\pi/2$ -pulse is no longer a transfer-pulse. This is understandable, bearing in mind that we want to preserve the induced phase shift and a transfer-pulse would be robust against the static

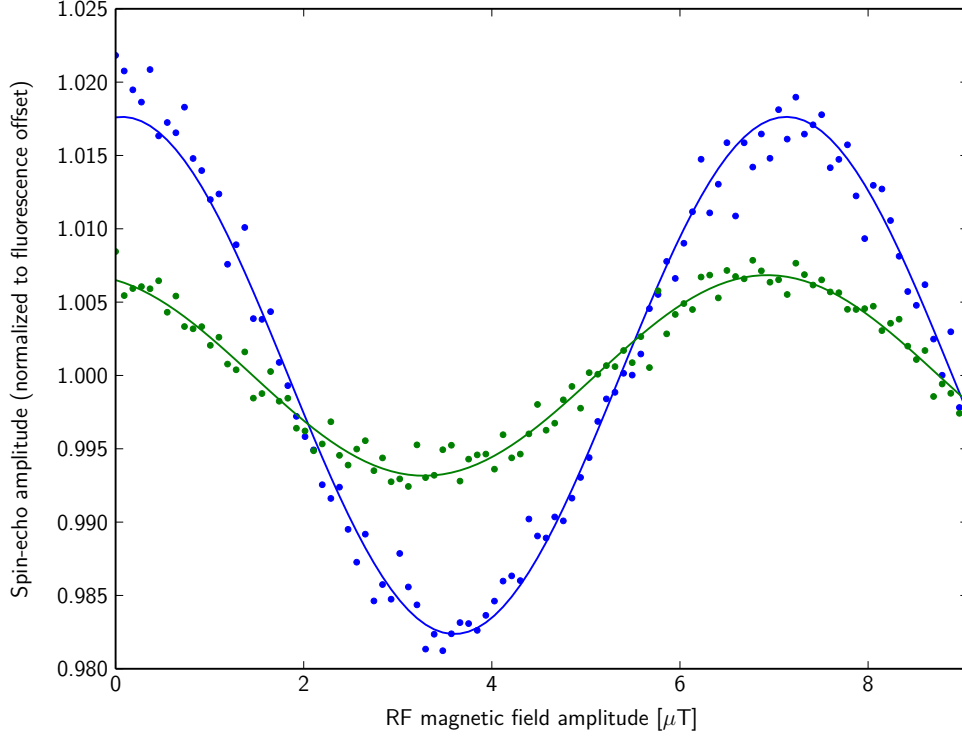


Figure 5.2: Experimental results for the sensing scheme using an ensemble of inhomogeneously broadened spins. The data points and cosine fits show the resulting modulation of the spin echo amplitude with increasing applied magnetic field for hard pulses (green) and SOC pulses (blue). When using SOC pulses, the contrast is improved by a factor two due to smaller pulses errors. The magnetic field labeled on the x -axis is not measured, but calculated using Eq. 5.2.

detuning induced by the applied magnetic field. Thus an operator- $\pi/2$ -pulse rotating the spins around the y -axis, which preserves the induced phase shift, is used.

Fig. 5.2 shows the experimental data, comparing a measurement with rectangular pulses to a measurement with SOC-pulses. The blue trace indicates measurements with SOC pulses, whereas the green one shows a measurement with simple rectangular pulses. The spin-echo contrast increases roughly the same value as for the spin-echo measurements in Sec. 4.4.2. The decrease in sensitivity is then inversely proportional to this increase in contrast.

The theoretical value from Eq. 5.9, the semi-theoretical approach, and the experimental value for the sensitivity yield roughly the same number, given in Tab. 5.1, which sums up the calculated and measured values of the sensitivity. The achieved sensitivity however is worse than in other measurements with ensembles of NV centers (see for

Table 5.1: Calculated S_{theo} and S_{semi} sensitivity compared to experimentally achieved sensitivity S_{exp} all given in $[\text{nT Hz}^{-1/2} \text{cm}^{-3/2}]$, using SOC-pulses and rectangular pulses

| | S_{theo} | S_{semi} | S_{exp} |
|--------------------|------------|------------|-----------|
| SOC-pulses | 1970 | 1840 | 1620 |
| rectangular-pulses | 4210 | 4180 | 4190 |

example Ref. [Tay08]), due to the limits that are given by the sample (bad ODMR contrast and relatively short dephasing times).

5.2 Wide-field magnetic sensing

Using ensembles of NV centers offers another advantage over using single NV centers: While the single NV center is great when using it as a point-like sensor, it is not possible to sense magnetic fields over a larger area at a time. On the contrary ensembles of NV centers offer the possibility to do exactly this, by looking at the response to a magnetic field of spatially distributed NV centers. This can be done by using a CCD camera and an objective with lower numerical aperture, which enables to illuminate and read-out the fluorescence of a larger area of the diamond at the same time, instead of the pointwise detection with the confocal microscope [Hon13].

Using the confocal microscope this behavior can be simulated by just laterally scanning over the NV sample, and carry out the magnetic sensing scheme for a few points along the way. By doing so, we move away from the wire, which carries the MW signal, and therefore the achievable Rabi frequency reduces (the amplitude of the magnetic field of a wire scales with $1/r$). When using rectangular pulses this change in Rabi-frequency decreases the sensitivity, since the pulse errors are becoming larger and reduce the contrast.

The SOC-pulses however are designed to be robust for a change in control amplitude. Hence the pulses are well suited to sense magnetic fields over a large area with the (almost) same sensitivity.

The sample we used for this experiment was different to the sample used in the prior section: In order to get high ODMR contrast and long dephasing times, a sample with few NV centers was used. In this sample a thin layer (≈ 20 nm) of NV centers was produced by irradiating a diamond with ^{14}N ions with a specific energy of 8 keV. This sample offers ODMR contrast comparable to a single NV center ($\approx 10\%$, when looking at one of the four NV species) and T_2 dephasing times in the range of several microseconds. This allows us to measure magnetic fields down to $\approx 100 \text{ nT Hz}^{-1/2} \text{cm}^{-3/2}$.

Figs. 5.3a and 5.3b show the results of this measurement, comparing a measurement with hard pulses to a measurement with SOC-pulses. The y -axis indicates the distance from the wire which carries the microwave signal, depicted as a drop in Rabi-frequency, while the x -axis shows an increasing B -field that results in an effective detuning. This field was additionally turned on, in order to increase the inhomogeneity and simulate

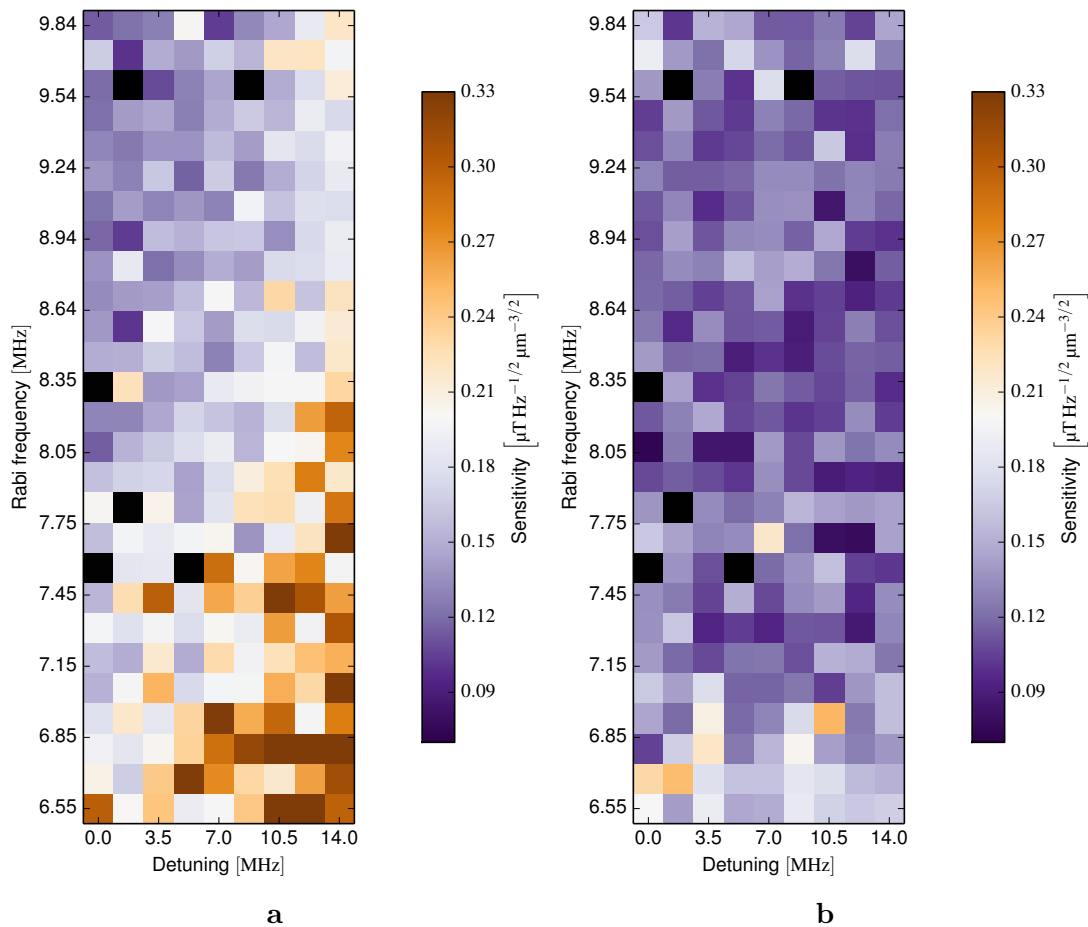


Figure 5.3: These figures show the sensing scheme as introduced in 5.1 yielding the sensitivities over a larger area. By moving away from the MW carrying wire the Rabi-frequency drops, the pulse errors increase and the sensitivity increases accordingly. An additional magnetic field increases the pulse errors by inducing an effective detuning. The black pixels in the plots are invalid data points where the sensing scheme did not work. This happened because of "holes" in the NV layer with no or very little NV-centers and thus very bad statistics when compared to "regular" points.

inhomogenously broadened spin ensembles. The results show that, when using SOC-pulses instead of rectangular pulses it enables us to sense magnetic fields of a large area with almost the same sensitivity.

6 Conclusion and outlook

Compared to other optimal control techniques, the pulses generated using the smooth optimal control algorithm are superior in many ways and can be used in a variety of different and new parts of physics.

The last part of this thesis shows only one of the possible fields of applications: magnetic field sensing. A lot of other scenarios suitable for the pulses are imaginable. For example the pulses should be very well suited for experiments concerning microwave resonators, since only signals within a very narrow bandwidth window are transmitted in such a resonator, thus a perfect application for our pulses.

Apart from that a lot of improvements still can be made concerning magnetic field sensing. Not only DC sensitive measurement schemes may be implemented easily (in fact that is even more basic than the presented AC sensing scheme), but also the sensitivity itself could be decreased by using “better” samples: Ensembles of spins with a T_2 time comparable to a single NV center, but still a large amount of fluorescence, could combine very low sensitivity, to the single digit nT regime as in Ref. [Pha11], with the same robustness concerning microwave powers and/or inhomogeneities in the local magnetic field as described in Sec. 5.

This could lead to possible applications in neuro-science: Using the NV-center as a pointlike magnetic sensor to image local magnetic fields with the pulses guaranteeing robustness in this inhomogeneous environment. This would possibly lead to a novel understanding of biology, exploring the quantum mechanical behavior of living cells.

Bibliography

- [Aco10] V. M. Acosta, A. Jarmola, E. Bauch, and D. Budker: *Optical properties of the nitrogen-vacancy singlet levels in diamond*. arXiv e-print 1009.0032. Phys. Rev. B 82, 201202(R) (2010). Aug. 2010 (cit. on pp. 8–10).
- [Alb13] A. Albrecht, A. Retzker, F. Jelezko, and M. B. Plenio: ‘Coupling of nitrogen vacancy centres in nanodiamonds by means of phonons’. In: *New Journal of Physics*, vol. 15(8) (Aug. 2013): p. 083014. DOI: [10.1088/1367-2630/15/8/083014](https://doi.org/10.1088/1367-2630/15/8/083014) (cit. on p. 13).
- [Asl13] N Aslam, G Waldherr, P Neumann, F Jelezko, and J Wrachtrup: ‘Photo-induced ionization dynamics of the nitrogen vacancy defect in diamond investigated by single-shot charge state detection’. In: *New Journal of Physics*, vol. 15(1) (Jan. 2013): p. 013064. DOI: [10.1088/1367-2630/15/1/013064](https://doi.org/10.1088/1367-2630/15/1/013064) (cit. on p. 8).
- [Bar13] Björn Bartels and Florian Mintert: ‘Smooth optimal control with Floquet theory’. In: *Physical Review A*, vol. 88(5) (Nov. 2013): p. 052315. DOI: [10.1103/PhysRevA.88.052315](https://doi.org/10.1103/PhysRevA.88.052315) (cit. on pp. 1, 27, 30).
- [Bla13] Martin Blaha: ‘Calibration of IQ Modulators’. Bachelor thesis. Technical University Vienna, 2013 (cit. on p. 37).
- [Bre07] Heinz-Peter Breuer and F Petruccione: *The theory of open quantum systems*. Oxford University Press, 2007 (cit. on p. 30).
- [Chi06a] L. Childress, M. V. G. Dutt, J. M. Taylor, A. S. Zibrov, F. Jelezko, J. Wrachtrup, P. R. Hemmer, and M. D. Lukin: ‘Coherent dynamics of coupled electron and nuclear spin qubits in diamond’. In: *Science*, vol. 314(5797) (2006): pp. 281–285 (cit. on pp. 7, 13).
- [Chi06b] Lilian Isabel Childress: ‘Coherent manipulation of single quantum systems in the solid state’. In: *Science*, vol. 314(5797) (2006): pp. 281–285 (cit. on p. 9).
- [Chu97] Isaac L. Chuang and M. A. Nielsen: ‘Prescription for experimental determination of the dynamics of a quantum black box’. In: *Journal of Modern Optics*, vol. 44(11-12) (1997): pp. 2455–2467. DOI: [10.1080/09500349708231894](https://doi.org/10.1080/09500349708231894) (cit. on pp. 49, 50).
- [Coh05] Claude Cohen-Tannoudji, Susan Reid Hemley, and Claude Cohen-Tannoudji: *Quantum mechanics*. Wiley, 2005 (cit. on pp. 3, 5).

- [Dav76] G. Davies: ‘The A nitrogen aggregate in diamond-its symmetry and possible structure’. In: *Journal of Physics C: Solid State Physics*, vol. 9(19) (Oct. 1976): p. L537. DOI: [10.1088/0022-3719/9/19/005](https://doi.org/10.1088/0022-3719/9/19/005) (cit. on p. 7).
- [Doh10] Marcus W. Doherty, Neil B. Manson, Paul Delaney, and Lloyd C. L. Hollenberg: *The negatively charged nitrogen-vacancy centre in diamond: the electronic solution*. arXiv e-print 1008.5224. *New J. Phys.* 13 (2011) 025019. Aug. 2010 (cit. on p. 8).
- [Dol11] F. Dolde, H. Fedder, M. W. Doherty, T. Nöbauer, F. Rempp, G. Balasubramanian, T. Wolf, F. Reinhard, L. C. L. Hollenberg, F. Jelezko, and J. Wrachtrup: ‘Electric-field sensing using single diamond spins’. In: *Nature Physics*, vol. 7(6) (June 2011): pp. 459–463. DOI: [10.1038/nphys1969](https://doi.org/10.1038/nphys1969) (cit. on pp. 14, 61).
- [Dr11] A. Dréau, M. Lesik, L. Rondin, P. Spinicelli, O. Arcizet, J.-F. Roch, and V. Jacques: ‘Avoiding power broadening in optically detected magnetic resonance of single NV defects for enhanced dc magnetic field sensitivity’. In: *Physical Review B*, vol. 84(19) (Nov. 2011): p. 195204. DOI: [10.1103/PhysRevB.84.195204](https://doi.org/10.1103/PhysRevB.84.195204) (cit. on p. 59).
- [Fox06] Mark Fox: *Quantum optics: an introduction*. Oxford master series in physics 15. Oxford University Press, 2006 (cit. on pp. 3, 4, 18).
- [Fu07] Chi-Cheng Fu, Hsu-Yang Lee, Kowa Chen, Tsong-Shin Lim, Hsiao-Yun Wu, Po-Keng Lin, Pei-Kuen Wei, Pei-Hsi Tsao, Huan-Cheng Chang, and Wun-shain Fann: ‘Characterization and application of single fluorescent nanodiamonds as cellular biomarkers’. In: *Proceedings of the National Academy of Sciences*, vol. 104(3) (Jan. 2007). PMID: 17213326: pp. 727–732. DOI: [10.1073/pnas.0605409104](https://doi.org/10.1073/pnas.0605409104) (cit. on p. 1).
- [Gao08] Jiansong Gao: ‘The physics of superconducting microwave resonators’. phd. California Institute of Technology, 2008 (cit. on p. 36).
- [Gol96] Gene H. Golub: *Matrix computations*. 3rd ed. Johns Hopkins studies in the mathematical sciences. Johns Hopkins University Press, 1996 (cit. on p. 52).
- [Hon13] Sungkun Hong, Michael S. Grinolds, Linh M. Pham, David Le Sage, Lan Luan, Ronald L. Walsworth, and Amir Yacoby: ‘Nanoscale magnetometry with NV centers in diamond’. In: *MRS Bulletin*, vol. 38(02) (2013): pp. 155–161. DOI: [10.1557/mrs.2013.23](https://doi.org/10.1557/mrs.2013.23) (cit. on p. 64).
- [How06] M. Howard, J. Twamley, C. Wittmann, T. Gaebel, F. Jelezko, and J. Wrachtrup: ‘Quantum process tomography and Linblad estimation of a solid-state qubit’. In: *New Journal of Physics*, vol. 8(3) (Mar. 2006): p. 33. DOI: [10.1088/1367-2630/8/3/033](https://doi.org/10.1088/1367-2630/8/3/033) (cit. on pp. 44, 51, 52).

- [Jam72] A. Jamiokowski: ‘Linear transformations which preserve trace and positive semidefiniteness of operators’. In: *Reports on Mathematical Physics*, vol. 3(4) (Dec. 1972): pp. 275–278. DOI: [10.1016/0034-4877\(72\)90011-0](https://doi.org/10.1016/0034-4877(72)90011-0) (cit. on p. 49).
- [Jel06] F. Jelezko and J. Wrachtrup: ‘Single defect centres in diamond: A review’. In: *physica status solidi (a)*, vol. 203(13) (Oct. 2006): pp. 3207–3225. DOI: [10.1002/pssa.200671403](https://doi.org/10.1002/pssa.200671403) (cit. on pp. 7, 13).
- [Joh13] J.R. Johansson, P.D. Nation, and Franco Nori: ‘QuTiP 2: A Python framework for the dynamics of open quantum systems’. In: *Computer Physics Communications*, vol. 184(4) (Apr. 2013): pp. 1234–1240. DOI: [10.1016/j.cpc.2012.11.019](https://doi.org/10.1016/j.cpc.2012.11.019) (cit. on p. 31).
- [Kir70] Donald E Kirk: *Optimal control theory; an introduction*. Prentice-Hall, 1970 (cit. on p. 27).
- [Kow13] Adrian Kowar: ‘Microwave microstructures for enhanced coherent control of nitrogen vacancy centre spin qubits in diamond’. MA thesis. University of Vienna, 2013 (cit. on pp. 17, 22, 55).
- [Lep11] G. Lepert, M. Trupke, M. J. Hartmann, M. B. Plenio, and E. A. Hinds: ‘Arrays of waveguide-coupled optical cavities that interact strongly with atoms’. In: *New Journal of Physics*, vol. 13(11) (Nov. 2011): p. 113002. DOI: [10.1088/1367-2630/13/11/113002](https://doi.org/10.1088/1367-2630/13/11/113002) (cit. on p. 1).
- [Maj07] J. Majer, J. M. Chow, J. M. Gambetta, Jens Koch, B. R. Johnson, J. A. Schreier, L. Frunzio, D. I. Schuster, A. A. Houck, A. Wallraff, A. Blais, M. H. Devoret, S. M. Girvin, and R. J. Schoelkopf: ‘Coupling superconducting qubits via a cavity bus’. In: *Nature*, vol. 449(7161) (Sept. 2007): pp. 443–447. DOI: [10.1038/nature06184](https://doi.org/10.1038/nature06184) (cit. on p. 1).
- [Man06] N. B. Manson, J. P. Harrison, and M. J. Sellars: *The nitrogen-vacancy center in diamond re-visited*. arXiv e-print cond-mat/0601360. Jan. 2006 (cit. on pp. 1, 7).
- [Maz08] J. R. Maze, P. L. Stanwix, J. S. Hodges, S. Hong, J. M. Taylor, P. Cappellaro, L. Jiang, M. V. Gurudev Dutt, E. Togan, A. S. Zibrov, A. Yacoby, R. L. Walsworth, and M. D. Lukin: ‘Nanoscale magnetic sensing with an individual electronic spin in diamond’. In: *Nature*, vol. 455(7213) (Oct. 2008): pp. 644–647. DOI: [10.1038/nature07279](https://doi.org/10.1038/nature07279) (cit. on p. 59).
- [Mes70] R. P. Messmer and G. D. Watkins: ‘Linear Combination of Atomic Orbital-Molecular Orbital Treatment of the Deep Defect Level in a Semiconductor: Nitrogen in Diamond’. In: *Physical Review Letters*, vol. 25(10) (Sept. 1970): pp. 656–659. DOI: [10.1103/PhysRevLett.25.656](https://doi.org/10.1103/PhysRevLett.25.656) (cit. on p. 8).

- [Nb13a] Tobias Nöbauer: ‘Sensing, coherent coupling and optimal control with nitrogen-vacancy colour centres in diamond’. PhD thesis. Technical University Vienna, 2013 (cit. on pp. 10, 15, 27, 29, 30, 59).
- [Nb13b] Tobias Nöbauer, Kathrin Buczak, Andreas Angerer, Stefan Putz, Georg Steinhauser, Johanna Akbarzadeh, Herwig Peterlik, Johannes Majer, Jörg Schmiedmayer, and Michael Trupke: ‘Creation of ensembles of nitrogen-vacancy centers in diamond by neutron and electron irradiation’. In: *arXiv:1309.0453 [cond-mat, physics:quant-ph]*, vol. (Sept. 2013) (cit. on p. 53).
- [Nie00] Michael A. Nielsen: *Quantum computation and quantum information*. Cambridge University Press, 2000 (cit. on pp. 5, 7, 44, 45, 47, 49).
- [Pha13] Linh My Pham: ‘Magnetic Field Sensing with Nitrogen-Vacancy Color Centers in Diamond’. In: vol. (Sept. 2013). Engineering and Applied Sciences (cit. on p. 19).
- [Pha11] L. M. Pham, D. Le Sage, P. L. Stanwix, T. K. Yeung, D. Glenn, A. Trifonov, P. Cappellaro, P. R. Hemmer, M. D. Lukin, H. Park, A. Yacoby, and R. L. Walsworth: ‘Magnetic field imaging with nitrogen-vacancy ensembles’. In: *New Journal of Physics*, vol. 13(4) (Apr. 2011): p. 045021. DOI: [10.1088/1367-2630/13/4/045021](https://doi.org/10.1088/1367-2630/13/4/045021) (cit. on pp. 59, 61, 67).
- [Sme11] Benjamin Smeltzer, Lilian Childress, and Adam Gali: ‘ ^{13}C hyperfine interactions in the nitrogen-vacancy centre in diamond’. In: *New Journal of Physics*, vol. 13(2) (Feb. 2011): p. 025021. DOI: [10.1088/1367-2630/13/2/025021](https://doi.org/10.1088/1367-2630/13/2/025021) (cit. on p. 13).
- [Sta10] P. L. Stanwix, L. M. Pham, J. R. Maze, D. Le Sage, T. K. Yeung, P. Cappellaro, P. R. Hemmer, A. Yacoby, M. D. Lukin, and R. L. Walsworth: ‘Coherence of nitrogen-vacancy electronic spin ensembles in diamond’. In: *Physical Review B*, vol. 82(20) (Nov. 2010): p. 201201. DOI: [10.1103/PhysRevB.82.201201](https://doi.org/10.1103/PhysRevB.82.201201) (cit. on pp. 25, 57, 62).
- [Ste09] M. Steiner, P. Neumann, J. Beck, F. Jelezko, and J. Wrachtrup: *Universal enhancement of the optical readout fidelity of single electron spins*. arXiv e-print 0909.2783. PRB 81, 035205 (2010). Sept. 2009 (cit. on p. 10).
- [Sto51] G. G. Stokes: ‘On the Composition and Resolution of Streams of Polarized Light from different Sources’. In: *Transactions of the Cambridge Philosophical Society*, vol. 9 (1851): p. 399 (cit. on p. 44).
- [Tay08] J. M. Taylor, P. Cappellaro, L. Childress, L. Jiang, D. Budker, P. R. Hemmer, A. Yacoby, R. Walsworth, and M. D. Lukin: ‘High-sensitivity diamond magnetometer with nanoscale resolution’. In: *Nature Physics*, vol. 4(10) (Oct. 2008): pp. 810–816. DOI: [10.1038/nphys1075](https://doi.org/10.1038/nphys1075) (cit. on p. 64).

- [Vit01] N.V. Vitanov, B.W. Shore, L. Yatsenko, K. Böhmer, T. Halfmann, T. Rickes, and K. Bergmann: ‘Power broadening revisited: theory and experiment’. In: *Optics Communications*, vol. 199(14) (Nov. 2001): pp. 117–126. DOI: [10.1016/S0030-4018\(01\)01495-X](https://doi.org/10.1016/S0030-4018(01)01495-X) (cit. on p. 19).
- [Xin12] Hu Xin, Liu Gang-Qin, Xu Zhang-Cheng, and Pan Xin-Yu: ‘Influence of Microwave Detuning on Ramsey Fringes of a Single Nitrogen Vacancy Center Spin in Diamond’. In: *Chinese Physics Letters*, vol. 29(2) (Feb. 2012): p. 024210. DOI: [10.1088/0256-307X/29/2/024210](https://doi.org/10.1088/0256-307X/29/2/024210) (cit. on p. 24).

List of Figures

| | | |
|-----|--|----|
| 2.1 | | 3 |
| 2.2 | The representation of a two-level system with the Bloch-sphere. Any state $ \Psi\rangle$ lies on the surface of the Bloch-sphere defined by the two angles θ and ϕ | 6 |
| 2.3 | | 8 |
| 2.4 | Term scheme of the NV-center at room temperature. Solid lines indicate allowed electric dipole transitions (red for the transitions we are interested in, and blue for a transition between the two metastable states), magnetic dipole transitions are shown as dotted black lines. Nonradiative intersystem crossing transitions are shown as dashed orange arrows. Level lifetimes and approximate branching ratios are depicted in the figure as well, taken from Ref. [Aco10] | 9 |
| 2.5 | Fluorescence time traces under constant illumination showing the difference in fluorescence for the bright and dark state. The blue trajectory shows the $m_s = 0$ state, whereas the green trajectory the $m_s \pm 1$ state. These curves are recorded after integrating over a lot of sweeps in order to reduce shot-noise and get rather smooth data curves. | 11 |
| 2.6 | Term scheme of the NV-ground state fine- and hyperfine structure, due to the nuclear spin of the adjacent ^{14}N atom. An external magnetic field lifts the degeneracy of the $m_s = \pm 1$ states. Solid lines indicate allowed magnetic dipole transitions. | 12 |
| 2.7 | Term scheme of the NV-ground state fine- and hyperfine structure, due to the nuclear spin of the adjacent ^{13}C atom. An external magnetic field lifts the degeneracy of the $m_s = \pm 1$ states. Solid lines indicate allowed magnetic dipole transitions. A_{\parallel} can be up to 130 MHz for very close ^{13}C atoms. | 12 |
| 3.1 | | 15 |
| 3.2 | The microwave chain, providing the 2.87 GHz signal. Two switches multiplex two different sources and chop the signal. The IQ mixer modulates two baseband signals from the arbitrary-waveform generator onto the microwave carrier. The amplifier then amplifies this quadrature-modulated signal. | 17 |

| | | |
|-----|---|----|
| 3.3 | Hyperfine-resolved ODMR spectrum of the $m_s = -1$ to $m_s = 0$ transition of a single NV center. The hyperfine structure occurs due to coupling to an adjacent ^{14}N and one nearby ^{13}C nuclear spin. The six lines are fitted with 6 Lorentzians, giving the exact positions of the transition frequencies. | 20 |
| 3.4 | | 21 |
| 3.5 | | 24 |
| 3.6 | | 25 |
| 4.1 | An example π -transfer-pulse (performing a $ 0\rangle \rightarrow 1\rangle$ transition), using ten frequency components within a bandwidth of 25 MHz and a maximum control amplitude of 9.49 MHz. The pulse is robust for ± 4 MHz detuned spins and inhomogeneities in the control amplitude of 25% . . . | 31 |
| 4.2 | Different temporal simulations for the pulse depicted in Fig. 4.1 acting on 1000 spins with detunings of up to 10 MHz. The red curve is an averaged trajectory with no additional dephasing. The blue curve is an averaged trajectory with constant (uncorrelated) exponential dephasing and finally the green curve is an averaged trajectory with Ornstein-Uhlenbeck noise (finite correlation time). The trajectories are all normalized to $[0,1]$, since the trajectory does not reach zero in general with simulated dephasing. This normalization is necessary when comparing the model to experimental data, because the absolute values of the fluorescence for ensembles of NV centers are not well-defined. | 32 |
| 4.3 | These figures show the temporal evolution of several spins with different detunings (ranging from -8 MHz to 8 MHz given by the segmentation of the arrows), and three different control amplitudes from 90% to 110% (three different colors) on the Bloch-sphere. Note however, that each of the spins was simulated separately without additional dephasing | 33 |
| 4.4 | One of the resulting ellipse for the mixer calibration as described in the main text. The center of the ellipse gives directly the LO-leakage error. The dashed lines indicates the main axis of the ellipse, illustrating the quadrature-angle error, while the ratio a/b of the main axis give the amplitude deviation error. The different ellipses were recorded using different LO-powers, from -10 dBm to 20 dBm at a frequency of 2.87 GHz, showing the independence of the errors on the LO-power | 36 |
| 4.5 | Example of a pulse-correction, with DC-offset, quadrature angle error and amplitude deviation corrected, using the method described above. The blue lines are the uncorrected pulses for each channel, compared to the corrected red ones, after multiplying with the matrix in Eq. 4.33. The amplitudes of the pulses are given in units of Rabi-frequencies. . . . | 39 |
| 4.6 | "Spin-selection"-scheme. Details are given in the main text | 41 |

- 4.7 FID-measurement after the polarization with the “spin-selection” scheme. This was the exact same measurement with the same NV-center as in Fig. 3.5b, but fitted with only one sine. The measurement was done for a 1 MHz detuned driving field, to show the sinusoidal behavior and not only the exponential decay that would be present for a resonant measurement 42
- 4.8 Experimental data compared to theoretical simulations. The green line indicates the theoretical simulation with additional exponential dephasing with a time-constant of 3 μ s, and the experimental data as solid blue line. Note that this measurement was done with only one spin 43
- 4.9 Comparison of theoretical and experimental fidelity map. The color-scale shows the infidelity (i.e. performance) of the pulse for different detunings and control amplitudes. The scale ranges from 1 (100% infidelity) to 10^{-2} (values lower than that have been truncated). Note, that the high number of pixels in the experimental plot, leads to a very long measurement time (3-5 days depending on the number of sweeps and pixels), and hence does not allow us to further improve the shot-noise limited SNR. Nevertheless the agreement between experiment and simulation is fair, and may be even improved by longer measurements. 44
- 4.10 Quantum state tomography as described in the main text. On the four input states, as depicted in the picture, a π_x operation is applied. The blue lines indicate the fluorescence of the $m_s = 1$ and the superposition state of $m_s = 0$ and $m_s = \pm 1$, with the data normalized to $[0,1]$. Considering for example the input state $|0\rangle$, one gets after a π_x rotation $m_s = -1$ (fluorescence minimum), for the z -direction, and half the fluorescence for the two other directions respectively. With this knowledge and Eq. 4.37 and Eq. 4.43 one can then reconstruct the output states as necessary for the QST-technique 48
- 4.11 Quantum process tomography as described in the main text for a process inducing a π_x rotation. The height of the columns represents the complex amplitude of the corresponding matrix element of the process χ -matrix, whereas the color represents the complex phase. These two figures show two different measurements, Fig. 4.11a a process tomography measurement with a SOC- π_x pulse, played at 75% of the ideal control amplitude, whereas Fig. 4.11b shows the same measurement but with 100% control amplitude. Resulting fidelities are given in the main text 50

- 4.12 Evolution of the ensemble-averaged population in the $m_s = 0$ state during playback of a series of SOC pulses. The pulses were scaled in amplitude from 72% to 134%. The amplitude scaling factor is given to the right of the respective traces. The resulting contrast is given in terms of relative change in fluorescence in the rightmost column. There is no significant drop in contrast, showing that the pulses are robust for a change in amplitude, even for an ensemble of spins. Note that these curves are normalized to the highest and lowest values respectively, and are slightly smoothed in order not to normalize on noise 54
- 4.13 A scan performed on an ensemble of spins, for the same transfer π pulse as in the previous sections. Plotted is a range of “squeezed” trajectories, denoting that the pulses have been compressed, by the factor depicted on the right side in each row. The contrast improves significantly, because the pulses become shorter compared to the dephasing time. The green lines are simulations with simple exponential dephasing. The trajectories are normalized to the maximum contrast of all pulses, which occurs at a squeeze factor of 44%, with a contrast of 8% (compared to 30% for a single NV-center). Obviously the contrast does not increase for the last squeeze-factor, maybe due to the fact, that the achieved 8% contrast is already the maximum achievable contrast. 55
- 4.14 Spin-echo sequence comparing a measurement with rectangular pulses (black line) with a measurement for equally long SOC-pulses (red). The contrast roughly increases by a factor of two. Simulations has been done according to Ref. [Sta10], giving T_2 times of ~ 6000 ns. The lower trace is generated by using a $3\pi/2$ pulse at the end instead of a $\pi/2$ -pulse . . . 57
- 5.1 Measurement scheme for AC-field sensing using NV-centers. The scheme is basically a spin-echo sequence with the difference of the applied magnetic field (depicted as blue line). The induced phase shift $\Delta\phi$ is proportional to the area under the blue curve 60
- 5.2 Experimental results for the sensing scheme using an ensemble of inhomogeneously broadened spins. The data points and cosine fits show the resulting modulation of the spin echo amplitude with increasing applied magnetic field for hard pulses (green) and SOC pulses (blue). When using SOC pulses, the contrast is improved by a factor two due to smaller pulses errors. The magnetic field labeled on the x -axis is not measured, but calculated using Eq. 5.2. 63

- 5.3 These figures show the sensing scheme as introduced in 5.1 yielding the sensitivities over a larger area. By moving away from the MW carrying wire the Rabi-frequency drops, the pulse errors increase and the sensitivity increases accordingly. An additional magnetic field increases the pulse errors by inducing an effective detuning. The black pixels in the plots are invalid data points where the sensing scheme did not work. This happened because of "holes" in the NV layer with no or very little NV-centers and thus very bad statistics when compared to "regular" points. 65

Acknowledgments

If I compare my knowledge of the beginning of the year to my knowledge now, it shows how much I have learned in the previous year. This is of course not possible without help from others, and hence I want to thank the group members guiding me on my way. I would like to thank especially Dr. Tobias Nöbauer helping me tremendously achieving the results in this thesis and pointing me in the right directions. And since almost everything I've been working with has been designed by him, also giving me the opportunity to do this interesting work. Moreover I want to thank Dr. Johannes Majer for help and fruitful discussions, and of course Dr. Jörg Schmiedmayer the head of the group. But not only certain people, the whole group helped me a lot along my way, always lending a ear when I had problems and/or showing me other, respectively better ways to solve a specific problem.

All in all I can say, that I'm happy that I chose this institute for graduating from University giving me the possibility to do my best work so far. To sum up my thesis in terms of myself I really enjoyed being part of this group learning a lot of new things about quantum- atom- and solid state physics, optics and microwave usage as well as a lot of new things about programming. I really like how this thesis turned out to expand my horizon.